Dust depletion of metals from local to distant galaxies. II. Cosmic dust-to-metal ratio and dust composition

Christina Konstantopoulou, Annalisa de Cia, Cédric Ledoux, Jens-Kristian Krogager, Lars Mattsson, Darach Watson, Kasper E. Heintz, Céline Péroux, Pasquier Noterdaeme, Anja C. Andersen, et al.

To cite this version:

Christina Konstantopoulou, Annalisa de Cia, Cédric Ledoux, Jens-Kristian Krogager, Lars Mattsson, et al.. Dust depletion of metals from local to distant galaxies. II. Cosmic dust-to-metal ratio and dust composition. Astronomy & Astrophysics - A&A, 2024, 681, 10.1051/0004-6361/202347171 . insu-04479020

HAL Id: insu-04479020
https://insu.hal.science/insu-04479020v1

Submitted on 10 Mar 2024

A&A, 681, A64 (2024)
https://doi.org/10.1051/0004-6361/202347171

Astronomy & Astrophysics

Dust depletion of metals from local to distant galaxies

II. Cosmic dust-to-metal ratio and dust composition

Christina Konstantopoulou[1], Annalisa De Cia[1,2], Cédric Ledoux[3], Jens-Kristian Krogager[4], Lars Mattsson[5], Darach Watson[6,7], Kasper E. Heintz[6,7], Céline Péroux[2,8], Pasquier Noterdaeme[9], Anja C. Andersen[10,11], Johan P. U. Fynbo[6,7], Iris Jermann[6,12], and Tanita Ramburuth-Hurt[1]

[1] Department of Astronomy, University of Geneva, Chemin Pegasi 51, 1290 Versoix, Switzerland
e-mail: christina.konstantopoulou@unige.ch
[2] European Southern Observatory, Karl-Schwarzschild Str. 2, 85748 Garching bei München, Germany
[3] European Southern Observatory, Alonso de Córdova 3107, Vitacura, Casilla 19001, Santiago, Chile
[4] Centre de Recherche Astrophysique de Lyon, CNRS, Univ. Claude Bernard Lyon 1, 9 Av. Charles André, 69230 Saint-Genis-Laval, France
[5] Nordita, KTH Royal Institute of Technology and Stockholm University, Hannes Alfvéns väg 12, 106 91, Stockholm, Sweden
[6] Cosmic Dawn Center (DAWN), Copenhagen, Denmark
[7] Niels Bohr Institute, University of Copenhagen, Jagtvej 128, 2200 Copenhagen N, Denmark
[8] Aix Marseille Université, CNRS, LAM (Laboratoire d'Astrophysique de Marseille) UMR 7326, 13388 Marseille, France
[9] Institut d'Astrophysique de Paris, CNRS-SU, UMR 7095, 98bis bd Arago, 75014 Paris, France
[10] Niels Bohr Institute, University of Copenhagen, Øster Voldgade 5–7, 1353 Copenhagen K, Denmark
[11] Department of Astrophysical Sciences, Princeton University, Princeton, NJ 08544, USA
[12] DTU Space, Technical University of Denmark, Elektrovej 327, 2800 Kgs. Lyngby, Denmark

Received 13 June 2023 / Accepted 20 October 2023

ABSTRACT

The evolution of cosmic dust content and the cycle between metals and dust in the interstellar medium (ISM) play a fundamental role in galaxy evolution. The chemical enrichment of the Universe can be traced through the evolution of the dust-to-metal ratio (DTM) and the dust-to-gas ratio (DTG) with metallicity. The physical processes through which dust is created and eventually destroyed remain to be elucidated. We use a novel method to determine mass estimates of the DTM, DTG, and dust composition in terms of the fraction of dust mass contributed by element X ($f_{\rm M_X}$) based on our previous measurements of the depletion of metals in different environments (the Milky Way, the Magellanic Clouds, and damped Lyman-α absorbers (DLAs) towards quasars (QSOs) and towards gamma-ray bursts (GRBs)), which were calculated from the relative abundances of metals in the ISM through absorption-line spectroscopy column densities observed mainly from VLT/UVES and X-shooter, and HST/STIS. We also derive the dust extinction from the estimated dust depletion ($A_{\rm V,depl}$) for GRB-DLAs, the Magellanic Clouds, and the Milky Way, and compare it with the $A_{\rm V}$ estimated from extinction ($A_{\rm V,ext}$). We find that the DTM and DTG ratios increase with metallicity and with the dust tracer [Zn/Fe]. This suggests that grain growth in the ISM is the dominant process of dust production, at least in the metallicity range ($-2 \leq [{\rm M/H}]_{\rm tot} \leq 0.5$) and redshift range ($0.6 < z < 6.3$) that we are studying. The increasing trend in the DTM and DTG with metallicity is in good agreement with a dust production and evolution hydrodynamical model. Our data suggest that the stellar dust yield is much lower (about 1%) than the metal yield and thus that the overall amount of dust in the warm neutral medium that is produced by stars is much lower than previously estimated. The global neutral gas metallicity is decreasing over cosmic time and is traced similarly by quasar-DLAs and GRB-DLAs. We find that, overall, $A_{\rm V,depl}$ is lower than $A_{\rm V,ext}$ for the Milky Way and in a few lines of sight for the Magellanic Clouds, a discrepancy that is likely related to the presence of carbonaceous dust associated with dense clumps of cold neutral gas. For the other environments studied here, we find good agreement overall between the $A_{\rm V,ext}$ and $A_{\rm V,depl}$. We show that the main elements ($f_{\rm M_X} > 1\%$) that contribute to the dust composition, by mass, are O, Fe, Si, Mg, C, S, Ni, and Al for all the environments, with Si, Mg, and C being equivalent contributors. There are nevertheless variations in the dust composition depending on the overall amount of dust. The abundances measured at low dust regimes in quasar- and GRB-DLAs suggest the presence of pyroxene and metallic iron in dust. These results give important information on the dust and metal content of galaxies across cosmic times, from the Milky Way up to $z = 6.3$.

Key words. dust, extinction – galaxies: abundances – galaxies: evolution – galaxies: ISM – Local Group – quasars: absorption lines

1. Introduction

The interplay between the production of metals by stars and the formation and evolution of cosmic dust plays a fundamental role in the chemical enrichment of the interstellar medium (ISM). The cycle of exchanging material between stars, interstellar gas, and cosmic dust drives galactic evolution (Maiolino & Mannucci 2019). Nevertheless, direct observations of the chemical properties of the baryon cycle remain extremely challenging.

Metals are formed in stars and are ejected into the ISM by strong stellar winds and supernova explosions. More than 90% of the baryons are found in the gas phase at $z > 2$ (Péroux & Howk 2020). These metals in the ISM can be incorporated into the next generation of stars. While substantial amounts of metals are found in neutral gas, large fractions of these metals are instead locked into dust grains, an effect called dust depletion (Field 1974; Savage & Sembach 1996; Phillips et al. 1982; Savaglio et al. 2003; Jenkins 2009; De Cia et al. 2016; Roman-Duval et al. 2021). Potential channels for the production of dust are the cooling ejecta of supernovae (Dunne et al. 2003; Matsuura et al. 2015), grain growth in the ISM (Draine 2003; Mattsson et al. 2012; Dwek 2016; De Cia et al. 2016), and asymptotic giant branch (AGB) stars (Gail et al. 2009; Höfner & Olofsson 2018). Around 30% of the light in the Universe is re-radiated by dust grains in the infrared, altering the light that we observe (Calzetti et al. 1995; Witt & Gordon 2000). Dust is also necessary in the process of star formation, because it is an important direct coolant for star formation and acts as a catalyst for the production of molecular hydrogen (Hollenbach & Salpeter 1971; Hollenbach & McKee 1979). Therefore, characterizing the dust properties and also the cycle of metals between the dust and gas is of fundamental importance to our understanding of galaxy formation and evolution.

The fraction of metals in dust can be described by the dust-to-metal ratio, and another indicator of the dust content is the dust-to-gas ratio (Draine 2003). These ratios can help us understand the production and destruction mechanisms of the dust and its evolution; they can be used to estimate a number of dust properties, including the dust surface density (see Péroux et al. 2023) and the dust composition. One way to infer the dust composition is to observe the abundances of metals in the gas phase ISM through absorption-line spectroscopy, taking into account their depletion into dust grains (e.g., Roman-Duval et al. 2022a). In Konstantopoulou et al. (2022, hereafter Paper I), we characterized the dust depletion of 18 metals in the Milky Way, the Magellanic Clouds, QSO-DLAs, and GRB-DLAs using the ISM relative abundances of metals following the prescription of De Cia et al. (2016). Here we use the depletion estimates from Paper I to infer the dust properties, namely the dust-to-gas (DTG) and dust-to-metal (DTM) ratios, dust composition, and dust extinction in a wide range of galactic environments (the Milky Way, the Magellanic Clouds, QSO-DLAs, and GRB-DLAs) and study how they evolve over cosmic time.

The paper is organized as follows. In Sect. 2, we briefly present the samples and the method we used to obtain dust-depletion estimates. In Sect. 3, we infer the DTM, the DTG, the extinction, and dust composition from depletion. We discuss our results in Sect. 4, and finally summarize and conclude in Sect. 5.

Throughout the paper, we use a linear unit for the column densities N in terms of ions cm^{-2}. We refer to relative abundances of elements X and Y as $[X/Y] \equiv \log\frac{N(X)}{N(Y)} - \log\frac{N(X)_{\odot}}{N(Y)_{\odot}}$, where reference solar abundances are taken from Asplund et al. (2021) following the recommendations of Lodders et al. (2009) (see Table 1 in Paper I). We adopt a Λ cold dark matter cosmology (ΛCDM) with $H_0 = 67.7\,\mathrm{km\,s^{-1}\,Mpc^{-1}}$, $\Omega_M = 0.3$, and $\Omega_\Lambda = 0.7$ (Planck Collaboration VI 2020).

2. Data samples

In this section, we briefly present the observational sample that we use for our analysis and the method that is used to estimate the dust depletion of all the metals for the Milky Way, the Magellanic Clouds, and for high-redshift QSO-DLAs and GRB-DLAs. These can be found in more detail in Paper I.

In Paper I, we used a large compilation of metal column densities measured in a consistent way in the neutral ISM for the Milky Way, the Magellanic Clouds, QSO-DLAs, and GRB-DLAs to characterize the dust depletion of 18 metals (C, P, O, Cl, Kr, S, Ge, Mg, Si, Cu, Co, Mn, Cr, Ni, Al, Ti, Zn, and Fe). Our sample probes gas in a wide range of galaxy types and regions. QSO-DLAs trace gas-rich regions in the outskirts of galaxies (Prochaska et al. 2007; Fynbo et al. 2008), while GRB-DLAs probe the inner regions of galaxies hosting GRBs in a way more similar to the Milky Way and the Magellanic Cloud samples but at high redshifts.

The Milky Way sample is from Jenkins (2009), De Cia et al. (2021), Welty & Crowther (2010), and Phillips et al. (1982). The Large Magellanic Cloud (LMC) sample is from Roman-Duval et al. (2021), the Small Magellanic Cloud (SMC) is from Welty & Crowther (2010), Tchernyshyov et al. (2015), Jenkins & Wallerstein (2017), and the QSO-DLAs sample is from De Cia et al. (2016, 2018), Berg et al. (2015). We also use 36 GRB-DLAs from Savaglio et al. (2003), Shin et al. (2006), Prochaska et al. (2007), Piranomonte et al. (2008), Ledoux et al. (2009), D'Elia et al. (2011), Wiseman et al. (2017), Zafar & Møller (2019), Bolmer et al. (2019) and Saccardi et al. (2023), as compiled in Heintz et al. (2023), who also present three new GRB-DLAs.

The column densities are measured mainly from spectra obtained with UVES/VLT, X-shooter/VLT, and STIS/HST and were homogenized to the newest oscillator strengths, which are listed in Paper I. Details of the properties of the full sample are presented in Paper I.

3. Methods and results

3.1. Dust depletion measurements

In this work, we adopt the dust depletions of each metal from Paper I, which were estimated from the relative abundances of metals (De Cia et al. 2016) based on the fact that different metals have different tendencies to be incorporated into dust grains. We note that this is a different approach from that of Roman-Duval et al. (2021), who also derived dust properties based on depletions, but estimated the depletions from the observed abundances and assuming a given metallicity of the gas. Here we briefly present our method.

The depletion of an element X (δ_X) can be estimated from the relative abundances of two elements that have different refractory properties but follow each other nucleosynthetically. If X is a refractory element and Y is volatile (i.e., is not easily depleted into dust, like Zn) then the dust depletion of X can be expressed using the ratio of the two elements [X/Y]. De Cia et al. (2016) and Paper I relied on [X/Zn] and their relation to the dust tracer to estimate the depletion of X. To trace the overall amount of dust, we used the dust tracer [Zn/Fe]. Two corrections are applied: first the dependence on the depletion of Zn is removed by assuming $\delta_{Zn} = -0.27 \times [\mathrm{Zn/Fe}]$, which is derived from the Milky Way and QSO-DLAs (De Cia et al. 2016), and second, a correction is applied to account for nucleosynthesis effects, such as α-element enhancement and Mn underabundance, as described in Paper I.

The depletion of X correlates linearly with the dust tracer, such as [Zn/Fe], but others, such as [Si/Ti] or [O/Si], are possible and thus the dust depletion can then be expressed by a simple linear relation as,

$$\delta_X = A2_X + B2_X \times [\mathrm{Zn/Fe}], \tag{1}$$

where the $A2_X$ and $B2_X$ coefficients for all the metals are the results of the linear fits to the data and are presented in Table 4

Table 1. Coefficients $A2_X$ and $B2_X$ resulting from the linear fit $\delta_X = A2_X + B2_X \times$ [Zn/Fe] of the depletion sequences of metals presented in Paper I and P from Konstantopoulou et al. (2023).

Element X	$A2_x$	$B2_x$
C	0.00	-0.10 ± 0.10
P	0.08 ± 0.05	-0.26 ± 0.08
O	0.00	-0.20 ± 0.05
Cl	0.00	-0.12 ± 0.09
Kr	0.00	-0.04 ± 0.09
S	0.01 ± 0.02	-0.48 ± 0.04
Zn	0.00 ± 0.01	-0.27 ± 0.03
Ge	0.00	-0.40 ± 0.04
Mg	0.01 ± 0.03	-0.66 ± 0.04
Si	-0.04 ± 0.02	-0.75 ± 0.03
Cu	0.00	-0.73 ± 0.04
Co	0.00	-0.89 ± 0.19
Mn	0.07 ± 0.02	-1.03 ± 0.03
Cr	0.12 ± 0.01	-1.30 ± 0.01
Ni	0.07 ± 0.02	-1.31 ± 0.03
Fe	-0.01 ± 0.03	-1.26 ± 0.04
Al	0.00	-1.66 ± 0.35
Ti	-0.07 ± 0.03	-1.67 ± 0.04

of Paper I. These results are consistent with the findings of De Cia et al. (2016). In Paper I, the coefficients are estimated using two different assumptions on α-element enhancement and Mn underabundance in the Magellanic Clouds. Here we adopt the coefficients that were estimated using the assumption of constant α-element enhancement and Mn underabundance; these are reported in Table 1 for completeness.

3.2. Dust-to-metal and dust-to-gas mass ratios

The total abundance of element X can be expressed as

$$\left(\frac{N(\mathrm{X})}{N(\mathrm{H})}\right)_{\mathrm{tot}} = 10^{([\mathrm{X/H}]_\odot + [M/\mathrm{H}]_{\mathrm{tot}})}, \tag{2}$$

where $[\mathrm{X/H}]_\odot$ is the solar abundance of element X and $[\mathrm{M/H}]_{\mathrm{tot}}$ is the total dust-corrected metallicity of the gas.

The DTM mass ratio can then be calculated including all the metals, as

$$\mathrm{DTM} = \frac{M_{\mathrm{dust}}}{M_{\mathrm{metals}}} = \frac{\Sigma_{\mathrm{X_i}}\,(1 - 10^{\delta_{\mathrm{X}_i}})\,10^{[\mathrm{X}_i/\mathrm{H}]_\odot}\,W_{\mathrm{X}_i}}{\Sigma_{\mathrm{X_i}}\,10^{[\mathrm{X}_i/\mathrm{H}]_\odot}\,W_{\mathrm{X}_i}}, \tag{3}$$

where δ_X is the dust depletion of element X, which is taken from Paper I, and W_X the atomic weight of element X. The total dust-corrected metallicity of the gas $[\mathrm{M/H}]_{\mathrm{tot}}$ cancels out and thus the dust-to-metal ratio is estimated independently of the total metallicity[1]. The sum is over all metals that have an elemental abundance $12 + \log(\mathrm{X/H}) > 3$. In total, we use 29 metals, namely, C, P, O, Cl, Kr, S, Ge, Mg, Si, Cu, Co, Mn, Cr, Ni, Al, Ti, N, Ne, Ar, F, Na, K, Ga, V, Sc, Se, Li, Zn, and Fe. The abundance measurements of these metals are done in the neutral gas of the ISM in their dominant ionization state, which is mostly singly ionized. In some cases, certain elements should be volatile, although their depletion is not assessed in Paper I. In such cases (namely, N, Ne, Ar, F, Na, K, Ga, V, Sc, Se and Li), we assume that $\delta_X = 0$. These metals make only a small difference in the calculation of the DTM and DTG, but we include them because they contribute to the mass of the metals by summing their atomic weights in the denominator of Eq. (3). The calculation of the depletions using the method of relative abundances is based on the availability of Zn and Fe. Therefore, when Zn and/or Fe were not available, no estimate of the depletion was made in Paper I. In the cases where δ_X was not estimated in Paper I, but [Zn/Fe] was observed, we use the coefficients $A2_X$ and $B2_X$ listed in Table 1 to estimate the depletion of δ_X using Eq. (1). The dust depletion is typically defined as a negative number, because it removes metals from the gas phase. However, in a few cases, the observed [Zn/Fe] is slightly negative, and typically consistent with zero within the uncertainties. In such cases, the values of depletion (δ_X) that we would strictly derive from the [Zn/Fe] would be slightly positive, which would be nonphysical (i.e., the presence of dust removes metals from the gas phase and does not add them). We therefore assign zero depletion in such cases. For the cases of GRB-DLAs with no observed [Zn/Fe], we use the estimated $[\mathrm{Zn/Fe}]_{\mathrm{fit}}$ from Heintz et al. (2023) to calculate the expected depletions from the coefficients $A2_X$ and $B2_X$ listed in Table 1 and using Eq. (1). $[\mathrm{Zn/Fe}]_{\mathrm{fit}}$ is equivalent to the observed [Zn/Fe], but is derived from the abundances of all the available metals.

The DTG is the total dust mass relative to the total gas mass, and can be expressed as

$$\mathrm{DTG} = \frac{M_{\mathrm{dust}}}{M_{\mathrm{gas}}} = \mathrm{DTM} \times 10^{[\mathrm{M/H}]_{\mathrm{tot}}} \times Z_\odot, \tag{4}$$

where DTM is defined in Eq. (3), $[\mathrm{M/H}]_{\mathrm{tot}}$ is the total dust-corrected metallicity of the gas, and $Z_\odot = 0.0139$ is the solar metallicity taken from Asplund et al. (2021). Figures 1 and 2 show the DTM (top panel) and the DTG (bottom panel) with respect to the dust tracer [Zn/Fe] and the total dust-corrected metallicity $[\mathrm{M/H}]_{\mathrm{tot}}$, respectively, and for all the environments. Our measurements are given in Tables B.1–B.5.

3.3. Dust composition

We estimate the fraction of dust mass contributed by element X, f_{M_X} as

$$f_{M_X} = \frac{(1 - 10^{\delta_X})\,10^{[\mathrm{X/H}]_\odot}\,W_{\mathrm{X}}}{\Sigma_{\mathrm{X}_i}\,(1 - 10^{\delta_{\mathrm{X}_i}})\,10^{[\mathrm{X}_i/\mathrm{H}]_\odot}\,W_{\mathrm{X}_i}}, \tag{5}$$

where $[\mathrm{X/H}]_\odot$ is the solar abundance of element X, δ_X is the dust depletion of element X, and W_X is the atomic weight of element X[2].

Figure 3 shows the evolution of dust composition with [Zn/Fe] for the elements that contribute at least 1% to the dust composition ($f_{M_X} > 1\%$). In cases where a measurement of δ_X is unavailable for a given system, we calculate it from the measurements of dust depletion of a given metal. This is done using Eq. (1) and the coefficients presented in Table 1. This means that in such cases the measurements of the dust depletion are extrapolated from the general behavior of the other environments, and our estimates on the dust composition are indicative.

---

[1] We note that Eq. (3) is equivalent to Eq. (9) of Roman-Duval et al. (2022a), but the depletions are estimated from the observed abundances. In De Cia et al. (2016), the calculation of DTM is based on $(1–10^{\delta_X})$ and only for Fe.

[2] We note that Eq. (5) is equivalent to Eq. (12) of Roman-Duval et al. (2022a), but the depletions are estimated in a different way (see Sect. 3.1).

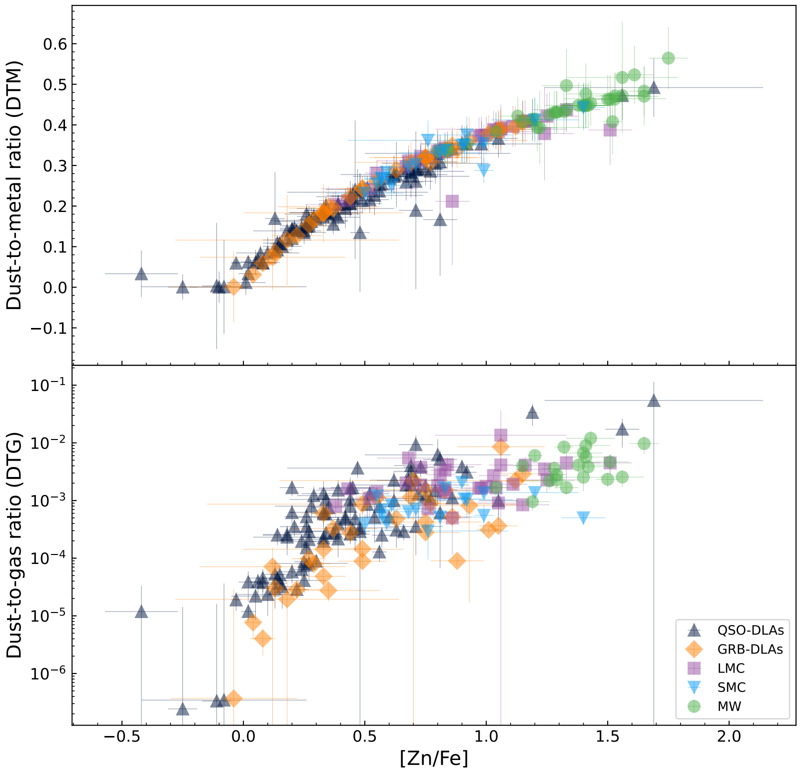

Fig. 1. Evolution of the dust-to-metal and dust-to-gas ratios with the amount of dust [Zn/Fe]. *Top*: Dust-to-metal ratio as a function of the dust tracer [Zn/Fe]. *Bottom*: Dust-to-gas ratio as a function of [Zn/Fe]. The black triangles are for QSO-DLAs, the purple squares are for the LMC, the blue triangles are for the SMC, the orange diamonds for the GRB-DLAs, and the green circles are for the Milky Way.

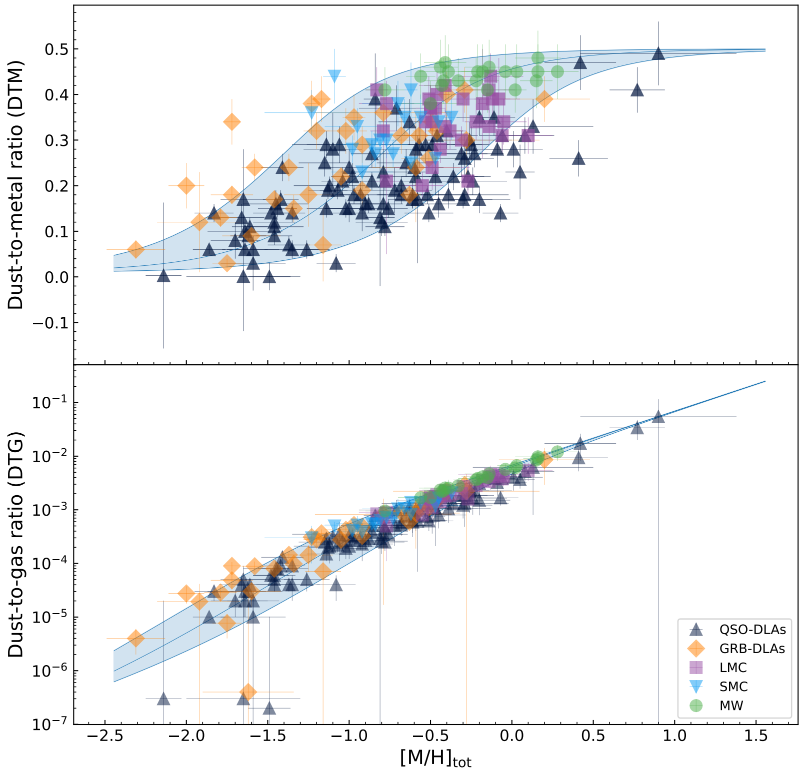

Fig. 2. Evolution of the dust-to-metal and dust-to-gas ratios with the total dust-corrected metallicity of the gas. *Top*: Dust-to-metal ratio as a function of the total dust-corrected gas metallicity $[M/H]_{tot}$. *Bottom*: Dust-to-gas ratio as a function of the total dust-corrected gas metallicity $[M/H]_{tot}$. The symbols are the same as in Fig. 1. For the Milky Way, metallicities $[M/H]_{tot}$ are from De Cia et al. (2021). There is a clear increasing trend in the DTM and DTG ratios with $[M/H]_{tot}$ and a tight correlation between DTG and $[M/H]_{tot}$. The blue shaded regions show the analytic dust production and evolution model tracks from Mattsson (2020) with varying the parameter $\delta = \epsilon$ from 1 to 16.

For the cases of targets that have less than three measurements of metals, the calculation of f_{M_X} is not reliable and therefore we exclude these targets. Figures A.2 to A.6 show the dust composition with respect to [Zn/Fe] for all the environments. The systems for which we have a measurement of dust depletion for each metal are shown with filled symbols and those calculated from the coefficients with empty symbols.

3.4. Dust extinction A_V from depletion

The extinction of light by dust grains depends on several factors, such as their density, size distribution, and composition (e.g., Draine 2003). While typically the dust extinction A_V is measured from the variations on the spectral continuum, it is also possible to estimate an A_V from the dust depletion (and the

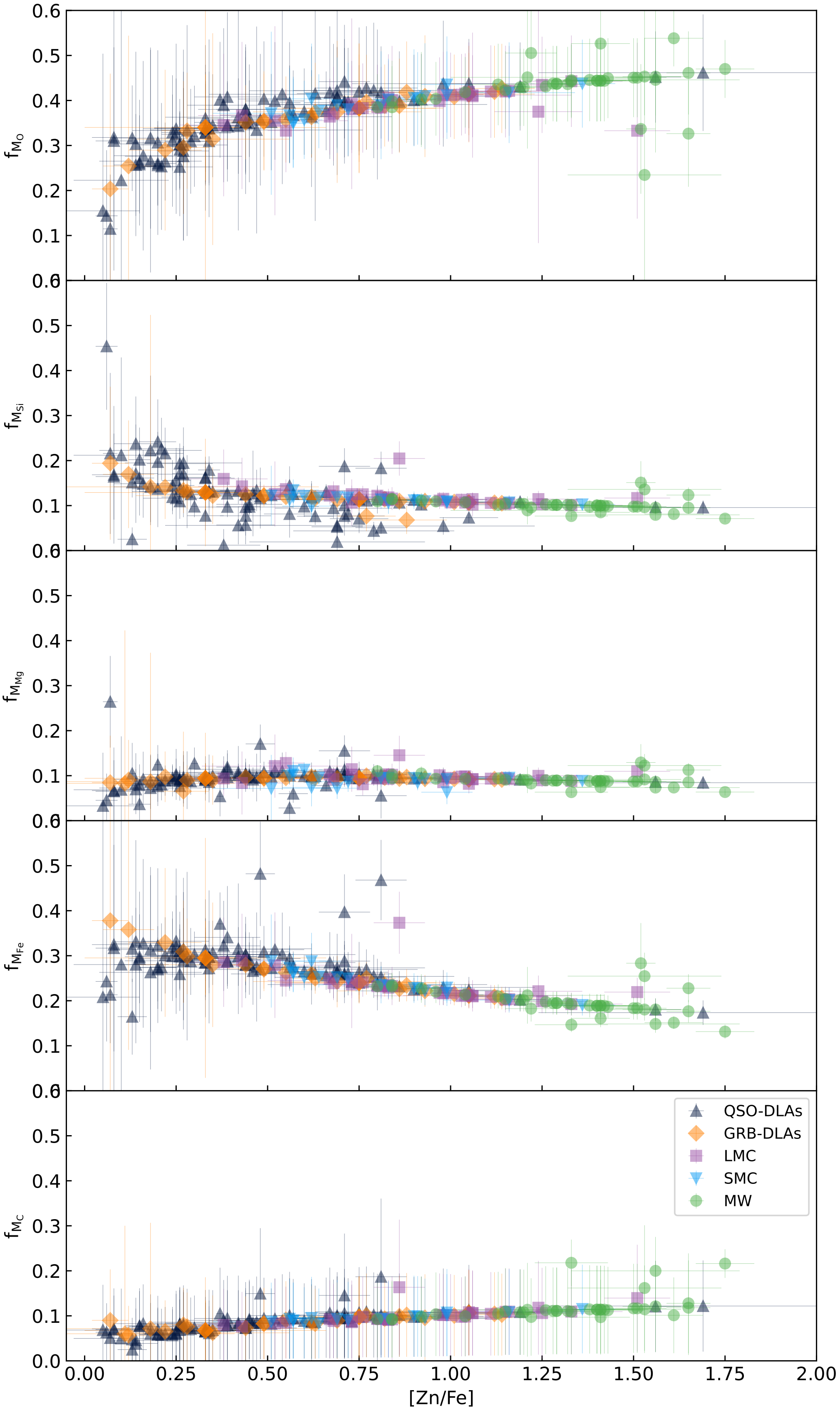

Fig. 3. Fraction of dust mass contributed by element X, f_{M_X} as a function of the dust tracer [Zn/Fe] for the five most abundant contributors in dust (O, Fe, Si, Mg, C) for QSO- and GRB-DLAs, LMC, SMC, and the Milky Way.

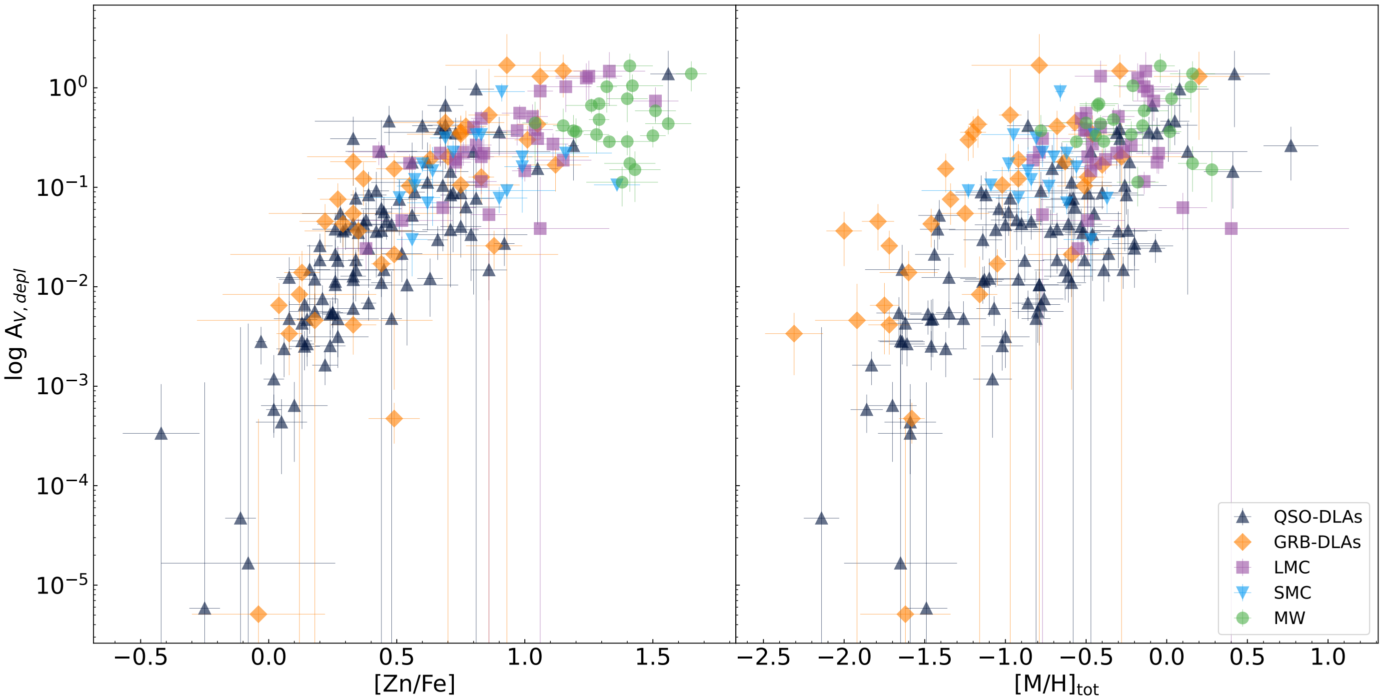

Fig. 4. Dust extinction $A_{\rm V,depl}$ as a function of [Zn/Fe] (left panel) and as a function of the total dust-corrected metallicity $[M/H]_{\rm tot}$ (right panel). For the Milky Way, metallicities $[M/H]_{\rm tot}$ are from De Cia et al. (2021).

dust-to-metals ratio), which we refer to as $A_{\rm V,depl}$. However, because dust extinction depends on the cross section of the dust grains, it is more sensitive to the number of grains than to the masses of the individual grains. Therefore, we derive the $A_{\rm V,depl}$ based on a DTM that is defined in terms of number of atoms (or column densities), which we refer to as $\rm DTM_N$. We derive the DTM in terms of column density by number as

$$\mathrm{DTM}_N = \frac{\Sigma_{\mathrm{X_i}}\,(1-10^{\delta_{\mathrm{X_i}}})\,10^{[\mathrm{X_i/H}]_\odot}}{\Sigma_{\mathrm{X_i}}\,10^{[\mathrm{X_i/H}]_\odot}}. \tag{6}$$

The DTM in terms of column density ($\rm DTM_N$) is on average 0.05 times lower than the DTM in terms of mass (DTM), as expected because Eq. (6) is equivalent to Eq. (3) without adding the atomic weights W_X of the elements. However, the overall trend is the same. Figure A.1 shows the relation between the DTM by mass and the DTM by column density ($\rm DTM_N$). Our measurements of both DTM and $\rm DTM_N$ are given in Tables B.1–B.5.

The dust extinction A_V can be derived from the depletion-estimated $\rm DTM_N$ as

$$A_{\rm V,depl} = \frac{\mathrm{DTM}_N}{\mathrm{DTM}_{N,\mathrm{Gal}}} \times \left(\frac{A_{\rm V}}{N(\mathrm{H})}\right)_{\rm Gal} \times N(\mathrm{H}) \times 10^{[\mathrm{M/H}]_{\rm tot}}, \tag{7}$$

where $\left(\frac{A_V}{N(H)}\right)_{\rm Gal} = 0.45 \times 10^{-21}$ mag cm^2 is the Galactic DTM ratio from Watson (2011). $\rm DTM_{N,Gal} = 0.354$ is the dust-to-metal ratio for the Galaxy in terms of column density, and is derived using Eq. (6) assuming an average [Zn/Fe] = 1.22 for the Milky Way. N(H) is the total column density of H, which is defined as $N(\mathrm{H}) = N(\mathrm{H\,I}) + 2\,N(\mathrm{H\,2})$, although only H I is measured for most QSO-DLAs and GRB-DLAs and H 2 is negligible (e.g., the mean molecular fraction measured in QSO-DLAs in Noterdaeme et al. 2008, is $\log f_{\rm H\,2} \sim -6.2$). $[M/H]_{\rm tot}$ is the total dust-corrected metallicity.

Figure 4 shows the distribution of $A_{\rm V,depl}$ with [Zn/Fe] (left panel) and with the total dust-corrected metallicity $[M/H]_{\rm tot}$ (right panel). The DTM, DTG, $\rm DTM_N$, and $A_{\rm V,depl}$ results for all the environments are reported in Tables B.1–B.5.

4. Discussion

4.1. DTM, DTG, and the origin of dust

The evolution of the DTM and DTG ratios with metallicity provides clues as to the origin of interstellar dust. The three candidate mechanisms for the formation of the bulk of cosmic dust are dust condensation in the envelopes of AGB stars (Gail et al. 2009), condensation in SNe ejecta (Dunne et al. 2003; Matsuura et al. 2015), and grain growth in the ISM (Draine 2003; Mattsson et al. 2012; Dwek 2016; De Cia et al. 2016).

Different dust-production mechanisms can produce different types of dust. AGB stars produce C-rich dust as well as silicates, while SNe produce mostly silicates. Type Ia SNe are the major Fe producers, but dust produced by Type Ia SNe has generally not been observed, with the exception of Dwek (2016) and Nagao et al. (2018). ISM grain growth by condensation upon existing seeds produced by stars is the mechanism that can produce both silicates and the observed amounts of C- and Fe-dust.

Different mechanisms of dust production have different dependencies on the environment metallicity. Dust that is mostly built up with ISM grain growth has DTM ratios that increase with metallicity, because the grain growth rate is metallicity dependent. On the other hand, SNe-produced dust should show a constant DTM (Mattsson et al. 2014), because dust production by SNe is weakly dependent on metallicity. AGB stars are often considered secondary for dust production, because of their longer lifetimes, although they cannot be neglected on short timescales (~500 Myr, Valiante et al. 2009).

Although grain growth in the ISM can occur at any time during the lifetime of a galaxy, Zhukovska et al. (2008) show that there is likely a critical metallicity above which grain growth in the ISM becomes dominant over other sources of dust production. Their evolution model shows that, at very low metallicities, that is, $[\mathrm{M/H}]_{\mathrm{tot}} \leq -2$, in the solar neighborhood the grain growth timescale exceeds the average lifetime of the molecular cloud by about 10 Myr. This means that until this point, very little is added to the dust content of the interstellar matter. When the metallicity of the ISM has reached $[\mathrm{M/H}]_{\mathrm{tot}} = -2$, some dust starts to condensate in the ISM and at $[\mathrm{M/H}]_{\mathrm{tot}} \sim -1$ the rate of growth increases rapidly and grain growth is the dominant mechanism of dust production in the diffuse ISM (Zhukovska et al. 2008). At high metallicities, such as in the Milky Way, the DTM ratio has a smaller dependence with metallicity. This is possibly because dust production depends not only on metallicity, but also on temperature, density, and pressure. In the Milky Way, the presence of cold dense gas and high pressure provide favorable conditions for the formation of dust. In this case, due to the higher dependence of ISM grain growth on density and pressure, the metallicity dependence is lower (Blitz & Rosolowsky 2006).

The top panel of Fig. 1 shows the DTM ratio with respect to the dust tracer [Zn/Fe] for the Milky Way, LMC, SMC, QSO-DLAs, and GRB-DLAs. It is evident that there is a tight correlation between the DTM and [Zn/Fe], which is expected given that the depletions that are used for the DTM calculation are linearly correlated with [Zn/Fe] (see Eq. (1)). The DTM is lower for QSO-DLAs and increases with increasing [Zn/Fe]; that is, for dustier systems, such as the Milky Way.

The bottom panel of Fig. 1 shows the DTG with respect to [Zn/Fe] for the Milky Way, LMC, SMC, QSO-DLAs, and GRB-DLAs. The DTG ratio is increasing with [Zn/Fe] and there is a larger scatter in the linear relation than that seen for the DTM (top panel of Fig. 1). Figure 2 shows the DTM (top panel) and DTG (bottom panel) with respect to the total dust-corrected metallicity $[\mathrm{M/H}]_{\mathrm{tot}}$. We find that, overall, the DTM is increasing with metallicity. For QSO-DLAs, we see a relatively sharp decline in the DTM at low metallicities (at $[\mathrm{M/H}]_{\mathrm{tot}} < -1$), indicating that the net dust-production rate is lower at low metallicities. This decline in the DTM could indicate that dust is more efficiently destroyed than it is formed in this low-metallicity regime. However, uncertainties are large for these few systems, probably as a result of the paucity of dust, which is difficult to measure with this method.

The analytic dust production and evolution model tracks from Mattsson (2020) are also shown in Fig. 2. The model is overplotted using Eq. (42) of Mattsson (2020) and assuming that the dust destruction parameter δ is equal to the growth parameter ϵ. The model considers all sources of dust, that is, stellar sources (AGB stars, SNe) and grain growth in the ISM, involves several simplifying assumptions, and is based on an idealised model of grain growth in turbulent cold molecular clouds. Some parameters are modified to fit the observational data well, that is, the stellar dust yield (y_{d}) is lowered by an order of magnitude with respect to Mattsson (2020) and the solar abundance $Z_{\odot}$ is updated to the most recent value from Asplund et al. (2021). The parameters for the model are then $y_Z = 0.01$, $y_{\mathrm{d}} = 1\times 10^{-4}$, $\delta = \epsilon$, and $Z_{\odot} = 0.0139$. The shaded regions in the plots show the parts of the DTM-$[\mathrm{M/H}]_{\mathrm{tot}}$ and DTG-$[\mathrm{M/H}]_{\mathrm{tot}}$ planes that are covered by varying $\delta = \epsilon$ from 1 to 16. Surprisingly, the predicted (stellar) dust yield is only 1% of the metals yield, while the previous estimates by Mattsson (2020) indicated 10%–20%. This suggests that the overall stellar population (and not individual cases) produces much less dust than previously estimated. We note that with our data we probe the integrated metals and dust recycled by the stellar sources (AGB stars, SNe) in the warm diffuse ISM. We might be missing the dust produced by stars in the dense and dustier regions around AGB stars or SNe.

The fact that the DTM is increasing with metallicity indicates that grain growth in the ISM is likely the dominant mechanism for dust production. This is supported by the fact that the data are a good fit to the dust production and evolution model trend from Mattsson (2020). We note that due to the nature of the measurements used in this paper (column densities of the metals in the warm neutral gas from UV absorption-line spectroscopy), there is a selection effect that privileges the sampling of environments where there is dust growth in the (more diffuse) ISM. Moreover, with the depletion measurements, we probably cannot distinguish between grain growth and dust destruction or sputtering in the diffuse ISM. With our method, we do not directly probe the very dense envelopes of AGB stars, or regions of condensation in SNe ejecta, but any dust that has been produced or recycled into the warm neutral ISM. In addition, the number of SNe or AGB stars along any given line of sight depends on the star-formation history of the local environment sampled. As shown in Paper I, the depletion sequences are independent of the star-formation histories of the different galaxies that were sampled. This means that the total budget of dust grains in the warm neutral medium does not depend on the star-formation histories of the galaxies. However, our technique does not probe dust in the densest regions of the ISM (cold and molecular neutral medium), and, in particular, the C-rich dust grains, which contribute significantly to the dust budget.

We find that the increase in DTM with metallicity does not develop at the same rate for all environments (49% increase for QSO-DLAs, 40% for GRB-DLAs, 23% for the LMC, 21% for the SMC, and 23% for the Milky Way). In environments with high metallicity and large amounts of cold dense gas (high pressure), as in the Milky Way disk, the dependence on the metallicity seems to become less important. In this case, grain growth in the ISM depends more strongly on pressure and thus molecular production and ISM grain growth (Blitz & Rosolowsky 2006). This can cause a shallower increase in the DTM with metallicity for environments with higher pressure.

Overall, the DTM is larger for dustier and higher-metallicity systems, such as the Milky Way, and is lower for QSO-DLAs. An increase in the DTM with metallicity has been observed in both local and distant galactic environments (e.g., De Cia et al. 2013, 2016; Wiseman et al. 2017), with this tendency somehow flattening above 0.1 $Z_{\odot}$ and reaching the Milky Way values. However, there are differences between the DTM calculations in these latter works. In our method, we use all the metals that contribute to dust, including C, by using the depletion of C that is estimated either from measurements for the Milky Way or from its empirical relation with [Zn/Fe] (calibrated with Milky Way data only) for the other environments. We also calculate the DTM in terms of mass, by weighting each element according to its atomic weight. De Cia et al. (2013, 2016) derive $\mathrm{DTM_N}$ in terms of column density and only based on the depletion of Fe. Wiseman et al. (2017) calculate the $\mathrm{DTM_N}$ in terms of column density and not including C. All these works refer to a normalized $\mathrm{DTM_N}$ with respect to the Milky Way. If we consider this, our $\mathrm{DTM_N}$ is consistent with the $\mathrm{DTM_N}$ estimated by Wiseman et al. (2017) within the uncertainties.

In Fig. 2, the DTM suggests that GRB-DLAs are dustier than QSO-DLAs for equal amounts of metals, while in Figs. 1 and 2 the DTG indicates that GRB-DLAs exhibit more gas with respect to QSO-DLAs along the lines of sight. In addition, most systems lying above the model expectations in Fig. 2 are GRB-DLAs at low metallicity, while those below are QSO-DLAs at

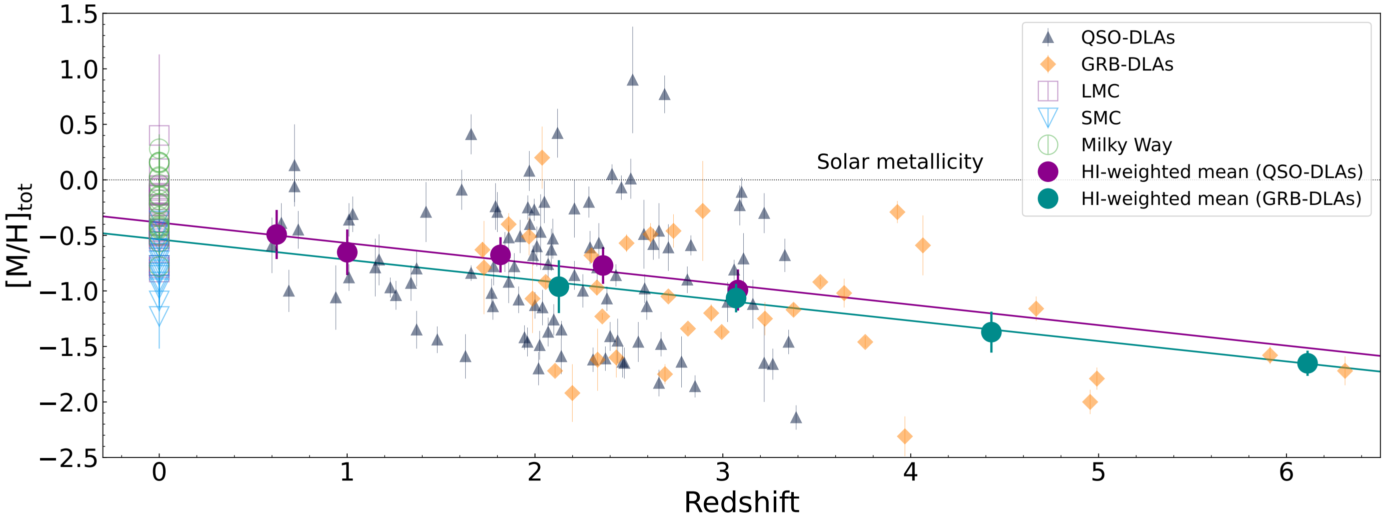

Fig. 5. Total dust-corrected metallicity $[\mathrm{M/H}]_{\mathrm{tot}}$ evolution with redshift z for QSO-DLAs (black triangles) and GRB-DLAs (orange diamonds). The larger points (purple for QSO-DLAs and green for GRB-DLAs) show the HI-weighted mean metallicities binned in redshift and the lines are their corresponding linear fits. The open symbols at redshift $z = 0$ refer to the Milky Way (green), the LMC (purple), and the SMC (blue). The dotted line shows the solar metallicity ($[\mathrm{M/H}]_{\mathrm{tot}} = 0$).

$[\mathrm{M/H}]_{\mathrm{tot}} > -0.3$. A possible explanation for these effects is the increased amount of colder dense gas and pressure in GRB hosts with respect to the more diffuse and warmer gas probed by QSO-DLAs. This is vastly a geometrical effect of GRB lines of sight crossing through more central parts of their host galaxy, while QSO-DLAs probe more peripheral regions of the absorbing galaxy (e.g., Fynbo et al. 2008; Krogager et al., in prep.). Overall, our results suggest that the production of dust is not only dependent on metallicity – or rather the availability of metals – but also on gas temperature, pressure, and density in each environment. The scatter that we observe in the DTM values at a given metallicity may be due to the different dynamical timescales over which the stellar and ISM sources contribute to dust at various redshifts. At higher redshifts, but for the same $[\mathrm{M/H}]_{\mathrm{tot}}$, it is possible that some sources did not have enough time to form dust in such short timescales (the Universe is only ~1 Gyr old at $z = 6$). The scatter in our DTM values suggests a complex interplay of factors within galactic environments. With our method, we primarily probe the characteristics of dust within the diffuse ISM. We acknowledge that our approach may not fully capture contributions from specific stellar sources, such as carbonaceous dust from AGB stars in denser regions. It is indeed possible that the scatter observed in our DTM values arises from the combined effects of sampling different combinations of more diffuse and denser ISM, as well as regions with varying star-formation histories. The results presented in Paper I indicate that in the diffuse ISM, dust origin appears to be less dependent on the star formation history of galaxies. As our study predominantly focuses on the diffuse ISM, we recognize the need for further research to explore methods that better represent denser regions, which may be influenced by variations in star formation history. The DTM overall tends to decrease with redshift, which is likely due to the dependence of the DTM on the decreasing metallicity (Heintz et al. 2023).

The DTG shows a clear increasing trend with metallicity for all the environments studied (see bottom panel of Fig. 2). The increase in DTG with metallicity has been consistently observed in previous works (Issa et al. 1990; Lisenfeld & Ferrara 1998; Draine & Li 2007; Galliano et al. 2008, 2018; Rémy-Ruyer et al. 2014; De Vis et al. 2017; Li et al. 2019; Roman-Duval et al. 2022b). The observed DTG trend with metallicity is in agreement with the dust production and evolution model from Mattsson (2020). Roman-Duval et al. (2022b) compare their observed DTG–metallicity trend with the model tracks from Feldmann (2015), which themselves are a good fit to the far-infrared (FIR) observations of galaxies presented by Rémy-Ruyer et al. (2014). In this comparison, Roman-Duval et al. (2022b) find a discrepancy between the QSO-DLA observations and the FIR observations from Rémy-Ruyer et al. (2014), which is still present in our current observational dataset. This discrepancy highlights the fact that FIR observations probe a very different kind of environment, likely the densest clouds around star-forming regions and AGB stars, which may contain dust of a different nature from what is observed in the diffuse ISM. The DTG–metallicity trend that we observe is consistent with that observed by Roman-Duval et al. (2022b).

4.2. Cosmic metallicity evolution of the neutral gas: Comparison between QSO-DLAs and GRB-DLAs

In Fig. 5, we compare the metallicity evolution with redshift between QSO-DLAs and GRB-DLAs. We calculate the H I-weighted mean from the linear metallicities in five redshift bins for QSO-DLAs and GRB-DLAs and plot the points at the mean redshift. We fit the H I-weighted mean metallicities, taking into account the y-axis uncertainties. The individual metallicity measurements in different environments are shown in Fig. 5. The two linear fits result in $[\mathrm{M/H}]_{\mathrm{tot}} = (-0.38 \pm 0.07) + (-0.18 \pm 0.03) \times z$ for QSO-DLAs and $[\mathrm{M/H}]_{\mathrm{tot}} = (-0.53 \pm 0.05) + (-0.18 \pm 0.01) \times z$ for GRB-DLAs, where z is the redshift. There is a small difference between the fits, which we quantify by calculating the difference between the reduced χ^2_ν of the two fits ($\Delta\chi^2_\nu = 0.04$). We note that the two samples have different redshift ranges, with most of the targets concentrating in the redshift range $1.8 < z < 3.2$. In this range, the observed scatter is large, and reflects the diversity in metallicity of galaxies at any given time. However, this is not complete, because optically and UV-selected QSOs tend to have lower $[\mathrm{M/H}]_{\mathrm{tot}}$, because their selection is biased by the presence of dust (Krogager et al. 2019). At higher and lower redshifts, there are fewer data points because of observational limitations. The effect of dust bias will be further investigated with the 4MOST–*Gaia* Purely Astrometric Quasar Survey (4G-PAQS; Krogager et al. 2023).

The H I-weighted mean metallicity is a measure of the metallicity in the neutral gas in the Universe rather than the metallicity of the individual systems. The agreement between the two fits suggests that QSO-DLAs and GRB-DLAs may arise from a similar population of galaxies, or at least probe the neutral gas in the Universe in a similar way (see also Krogager et al., in prep.). We find a decrease in neutral gas metallicity with redshift ($0.6 < z < 6.3$), which is in agreement with previous studies (e.g., De Cia et al. 2018; Mattsson et al. 2019; Péroux & Howk 2020). The inclusion of GRB-DLAs extends the study of the cosmic chemical evolution to $z > 6$ (Heintz et al. 2023; Saccardi et al. 2023).

4.3. Dust composition

Figure 3 shows the evolution of dust composition derived from the dust depletion, with [Zn/Fe] for the elements that contribute at least 1% of the dust composition ($f_{\rm M_X}$> 1%). Dust depletion can be used to obtain information on the dust composition in various ways (Savage & Sembach 1996; Jenkins 2014; De Cia et al. 2016; Mattsson et al. 2019; Roman-Duval et al. 2022a).

In each panel of Fig. 3, we can see that the main components of dust, by mass, are O, Fe, Si, Mg, C, S, Ni and Al. However, the distribution of the elements that compose dust varies with the amount of dust in the system measured with [Zn/Fe]. Figure 6 visualizes the distribution of metals that compose dust for the least dusty systems (upper panel: e.g., [Zn/Fe] < 0.3), the distribution of metals in the middle range of [Zn/Fe] (middle panel, e.g. 0.3 ≤ [Zn/Fe] ≤ 0.9) and for most dusty systems (lower panel, e.g., 0.9 < [Zn/Fe] < 1.2). Systems with low dust content ([Zn/Fe] < 0.3) are observed among QSO-DLAs and GRB-DLAs, which tend to have low metallicity. In these systems, the most abundant elements in dust are Fe and O, followed by Si. On the contrary, in the average [Zn/Fe] and high-dust-content regime (0.9 < [Zn/Fe] < 1.2), O is more abundant than Fe in all galactic environments. Overall, in GRB-DLAs and QSO-DLAs, the contribution of Fe and Si to dust increases steeply as we go towards lower [Zn/Fe] (i.e., less dust), while O decreases. We speculate that this least dusty regime may be one where the seeds of dust grains did not undergo as much grain growth by the gradual accumulation of matter in the ISM, because there was not enough time, or they underwent a more efficient dust-destruction process by SNe shocks. In low-metallicity environments with relatively little dust, the dust grains are small and are more easily destroyed by SNe shocks. The main dust-destruction processes in the ISM are either from sputtering by high-velocity SN shocks and photo-destruction by high-energy photons (Dwek et al. 1996; Jones et al. 1996; Bocchio et al. 2014; Slavin et al. 2015) or from consumption of interstellar dust by star formation (astration).

Table 2 presents the gas- and solid-phase abundances in parts per million (ppm) of the main elements that contribute to the dust composition for systems in different environments and for the three different intervals of [Zn/Fe] defined above. At low depletion levels ([Zn/Fe] < 0.3), where dust starts to form, we find for QSO-DLAs and GRB-DLAs that the O abundance in dust is approximately three times higher than the Si abundance. This suggests that the presence of pyroxene ($\mathrm{Mg_xFe_{(1-x)}SiO_3}$) is likely. The amounts of Fe and Mg observed in the least dusty regime suggest a significant contribution of enstatites ($\mathrm{MgSiO_3}$) and metallic Fe. There is no need to invoke oxydation of Fe (e.g., FeO) in the least dusty regime because all the oxygen can in principle be included in pyroxenes. A more detailed analysis of the dust composition, such as that presented in Mattsson et al. (2019), is required to accurately constrain the dust composition of the different environments.

The different environments considered in this study span different ranges of dust content ([Zn/Fe], see Fig. 3). Here, we discuss their average properties. For the full range of [Zn/Fe], and for all the environments, we find that the largest fraction of dust mass is contributed by O and is increasing with [Zn/Fe], with a smaller increase in the Milky Way and the largest increase for QSO-DLAs. The largest amount of O in dust is found in the Milky Way (44%) and the smallest is found in GRB-DLAs (35%). The second most abundant element in dust is Fe, which is decreasing with [Zn/Fe] for all the environments studied. A possible cause for the opposite evolutions of the mass abundance of O and C with respect to Fe and other refractory elements is the following. For the least dusty systems, at low levels of [Zn/Fe], most of the Fe and other refractory elements are available in the gas phase and are those that can more easily be incorporated into dust grains. On the other hand, for very dusty systems, at high levels of dust depletion, there are many fewer atoms of Fe and refractory metals available in the gas phase to form additional dust, while O and C are always very abundant in the gas phase. Layers of complexity will need to be added to this simplified picture when considering systems that have intrinsically very low abundances of Fe and heavily refractory metals; for example, in the very distant Universe. The chemical evolution of galactic environments and their local star-formation histories influence the availability of metals for dust formation. In regions with lower metallicity and lower dust content, which are chemically less evolved, there might be a reduced abundance of the heavy elements crucial for dust production. Si, C, Mg, S, Ni, and Al make smaller contributions to dust (<12%) in all the environments studied here. Table 3 presents the average percentages of the main elements that contribute to the dust composition for systems in different environments.

Our current data suggest that C has a similar mass abundance in dust for all the environments studied here; that is, 8%, 9%, 10%, 10%, and 12% for QSO-DLAs, GRB-DLAs, LMC, SMC, and the Milky Way, respectively. However, the Milky Way and Magellanic Clouds have substantially different extinction curves; in particular the presence and strength of the 2175 Å feature (e.g., Pei 1992). The origin of the 2175 Å feature remains unclear and it is likely the product of a combination of several species. Some candidates for its origin have been proposed, such as nongraphitic C (Mathis 1994) or polycyclic aromatic hydrocarbons (PAHs, Draine 2003). This indicates that the Milky Way has a much higher content of C-rich dust possibly in the form of PAHs (Shivaei et al. 2022) – than the LMC, and an even higher content compared to the SMC. The SMC extinction curve mostly does not show the 2175 Å feature, with few exceptions (e.g., Gordon & Clayton 1998; Gordon et al. 2003; Welty & Crowther 2010). Most GRB afterglows also do not show a 2175 Å feature in their extinction curve (e.g., Zafar et al. 2011; Schady et al. 2012), with some exceptions (Elíasdóttir et al. 2009; Zafar et al. 2012; Heintz et al. 2019). Therefore, one might expect a smaller contribution from PAH grains to the dust composition in GRBs, and possibly also a smaller contribution from C-rich dust, as well as smaller grain sizes. The distribution of PAHs may actually vary with location, being more strongly associated with

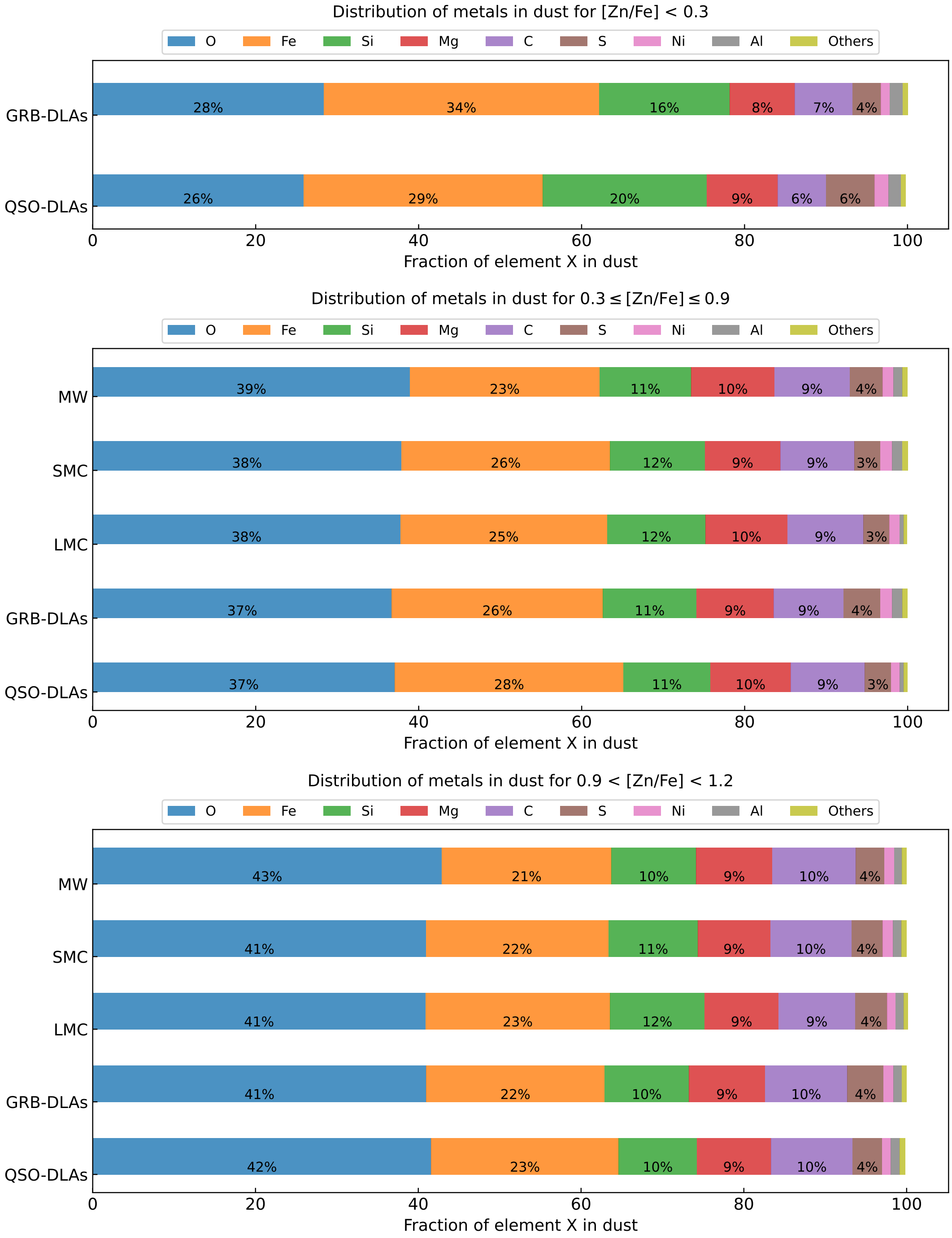

Fig. 6. Distribution of metals that compose dust for the main elements ($f_{\mathrm{M_X}} > 1\%$) that contribute to dust. The top, middle, and bottom panels show the distribution of elements for [Zn/Fe] < 0.3 in QSO-DLAs and GRB-DLAs, for 0.3 < [Zn/Fe] < 0.9 in all the environments, and for 0.9 < [Zn/Fe] < 1.2 in all environments, respectively.

molecular clouds (Sandstrom et al. 2010). The dust depletion analysis is a more efficient probe of the warm neutral medium in galaxies, and may not be particularly sensitive to dust located in dense molecular clouds. Therefore, our results on dust composition are only representative of the dust in the warm neutral medium, while the dust located in dense molecular clouds might be different in composition.

The depletion of C in dust is very uncertain for GRB-DLAs and QSO-DLAs because the typical C II line used to measure the C content is normally highly saturated. In Paper I, we derived the depletion of C based on only five Milky Way measurements, which can only provide a rough estimate of the C dust depletion. We extrapolate these estimates of C depletion to the other environments and this is probably the cause of the similar percentages of C dust composition that we obtain, regardless of the presence or not of strong C-dust features in their extinction curves (i.e., SMC, LMC). This highlights the need for a detailed study of C depletion as well as the need for more, and more reliable, measurements for systems in all environments.

Similar C fractions in dust can also result from the fact that most of the C is produced by C-rich AGB stars (Gustafsson et al. 1999; Mattsson 2010), the presence of which does not depend on the environment; although C-rich massive stars may significantly contribute to the C budget (Gustafsson 2022).

Table 2. Gas- and solid-phase abundances of the main elements that contribute to the dust composition for systems in different environments and for different intervals of [Zn/Fe].

Element X	$[X/H]_{gas}$ (ppm)	$[X/H]_{dust}$ (ppm)					Interval [Zn/Fe]
		QSO-DLAs	GRB-DLAs	Milky Way	LMC	SMC	
O	490	35	27	...	...	...	[Zn/Fe] < 0.3
		102	118	154	126	125	0.3 ≤ [Zn/Fe] ≤ 0.9
		186	178	181	172	168	0.9 < [Zn/Fe] < 1.2
Fe	29	10	27	...	...	...	[Zn/Fe] < 0.3
		23	23	26	25	25	0.3 ≤ [Zn/Fe] ≤ 0.9
		27	27	27	27	27	0.9 < [Zn/Fe] < 1.2
Si	32	13	8	...	...	...	[Zn/Fe] < 0.3
		14	20	25	25	22	0.3 ≤ [Zn/Fe] ≤ 0.9
		21	25	27	26	27	0.9 < [Zn/Fe] < 1.2
Mg	35	7	5	...	...	...	[Zn/Fe] < 0.3
		18	20	27	24	20	0.3 ≤ [Zn/Fe] ≤ 0.9
		24	27	28	22	26	0.9 < [Zn/Fe] < 1.2
C	288	10	8	...	...	...	[Zn/Fe] < 0.3
		34	37	48	43	40	0.3 ≤ [Zn/Fe] ≤ 0.9
		56	33	81	48	54	0.9 < [Zn/Fe] < 1.2
S	14	3	2	...	...	...	[Zn/Fe] < 0.3
		5	6	8	6	5	0.3 ≤ [Zn/Fe] ≤ 0.9
		7	10	8	8	9	0.9 < [Zn/Fe] < 1.2
Ni	2	1	0.3	...	...	...	[Zn/Fe] < 0.3
		1	1	1	1	1	0.3 ≤ [Zn/Fe] ≤ 0.9
		1	1	2	1	1	0.9 < [Zn/Fe] < 1.2
Al	3	1	1	...	...	...	[Zn/Fe] < 0.3
		2	2	3	3	2	0.3 ≤ [Zn/Fe] ≤ 0.9
		3	3	3	2	3	0.9 < [Zn/Fe] < 1.2

Table 3. Average percentage of the main elements that contribute to the dust composition for systems in different environments.

X	QSO-DLAs	GRB-DLAs	LMC	SMC	Milky Way
O	36%	35%	38%	39%	44%
Fe	27%	27%	23%	24%	19%
Si	11%	12%	12%	11%	10%
Mg	9%	9%	10%	9%	9%
C	8%	9%	10%	10%	12%
S	4%	4%	4%	3%	4%
Ni	2%	1%	1%	1%	1%
Al	1%	1%	1%	1%	1%

4.4. Dust extinction from depletion compared to extinction from SED

Figure 4 shows the distribution of $A_{V,depl}$ as a function of [Zn/Fe] (left panel) and as a function of the total dust-corrected metallicity $[M/H]_{tot}$ (right panel). The $A_{V,depl}$ for QSO-DLAs is generally small and increases with the dust tracer [Zn/Fe] and with the total dust-corrected metallicity $[M/H]_{tot}$. At higher metallicities and [Zn/Fe], the dust extinction is also expected to be higher. The right panel of Fig. 4 shows that, for a given metallicity, QSO-DLAs tend to have a lower $A_{V,depl}$ than the other systems. This is probably due to the fact that QSO-DLAs probe galactic regions that are further out than those probed by GRB-DLAs (Prochaska et al. 2007; Fynbo et al. 2008) and absorbing systems towards OB stars in local galaxies.

We compare the $A_{V,depl}$ with $A_{V,ext}$, which we measured from the reddening $A_V = E(B - V) \times R_V$, assuming $R_V = 3.08$ for the Milky Way , $R_V = 3.16$ for the LMC, and $R_V = 2.93$ for the SMC (Pei 1992). In the case of GRB-DLAs, we compare the $A_{V,depl}$ with the $A_{V,ext}$ measured from the SED in Heintz et al. (2023). The comparison between $A_{V,depl}$ and $A_{V,ext}$ is shown in Fig. 7. The green circles highlight systems in the Magellanic Clouds that show a 2175 Å feature in their dust-extinction curve. $A_{V,ext}$ is difficult to obtain for QSO-DLAs and no measurements are available for the systems that we are studying here. The dust extinction $A_{V,ext}$ of a sample of QSO-DLAs has been measured in previous studies (Krogager et al. 2016; Heintz et al. 2016), but such measurements are only possible for strong absorbers and/or for cases with the 2175 Å bump present in their spectra. We find that $A_{V,depl}$ is much lower than $A_{V,ext}$ for the Milky Way. This could be due to the fact that with $A_{V,depl}$ we are probing only the warm diffuse ISM, while $A_{V,ext}$ is the cumulative extinction along the full line of sight, including the warm ISM and also regions of cold dense gas. On the other hand, for the LMC, SMC, and GRB-DLAs, the $A_{V,depl}$ is generally in good agreement with $A_{V,ext}$, with some exceptions that lie above or below the 1:1 line of equality. In the LMC and the SMC, most of the systems lie below the line of equality ($A_{V,ext} > A_{V,depl}$). We quantify the correlation between the two measurements of A_V by calculating the

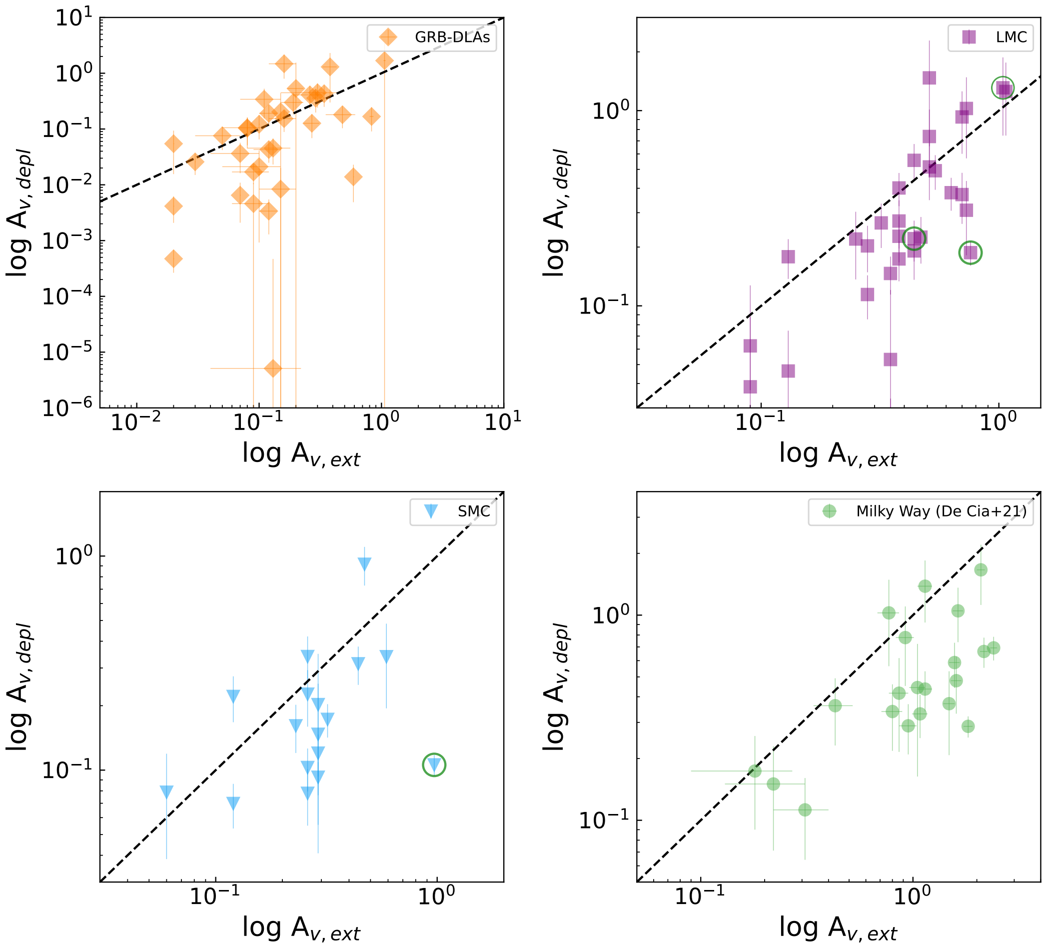

Fig. 7. Dust extinction A_V as measured from extinction against the A_V calculated using the dust depletion for GRB-DLAs, LMC, SMC, and the Milky Way. The black dashed line indicates the 1:1 conversion between the two. The green circles show targets with a 2175 Å feature or signs of carbonaceous dust.

χ^2_ν between $A_{V,\mathrm{ext}}$ and $A_{V,\mathrm{depl}}$ for all the environments studied here. The Milky Way has the highest χ^2_ν with $\chi^2_\nu = 2.18$, followed by the SMC with $\chi^2_\nu = 2.14$. GRB-DLAs have $\chi^2_\nu = 1.03$ and finally the LMC has $\chi^2_\nu = 0.63$. We additionally estimated the Pearson's correlation coefficients r and report: $r = 0.55$ (GRBs), $r = 0.71$ (LMC), $r = 0.30$ (SMC), and $r = 0.48$ (Milky Way). These indicate that the LMC points have the tightest correlation and the SMC the loosest. However, the low r for the SMC is driven only by the outlier marked in the green circle, which if excluded would give $r = 0.61$, which is because this point has different properties due to the presence of the 2175 Å bump in the dust-extinction curve for this system and is a physical outlier.

Savaglio & Fall (2004), Wiseman et al. (2017) and Bolmer et al. (2019) also compare their estimates of the dust extinction derived from depletion $A_{V,\mathrm{depl}}$ with the dust extinction derived from SED ($A_{V,\mathrm{ext}}$) for GRB-DLAs. These authors find that some systems lie above or below the line of equality, with an overall larger scatter that is observed in this paper, and they report that most lines of sight have a larger $A_{V,\mathrm{depl}}$ than $A_{V,\mathrm{ext}}$. The difference in our method is that we include C, in addition to several other metals in the derivation of $A_{V,\mathrm{depl}}$ (all those that have an elemental abundance of $12 + \log(\mathrm{X/H}) > 3$). Dust extinction depends on the composition of the dust, but also on the grain size distribution (Mathis et al. 1977; Pei 1992; Hoffman & Draine 2016; Mattsson 2020), and gray dust has previously been suggested (e.g., Wiseman et al. 2017) as a solution for the high $A_{V,\mathrm{depl}}$ but low reddening in some sources. If grains are big enough, then the extinction depends less on the wavelength and more on the geometrical cross section, which has been observed in some instances (e.g., Friis et al. 2015). In this case, the extinction curve is achromatic and $A_{V,\mathrm{ext}}$ would be lower because each measurement is sensitive only to wavelength-dependent extinction. On the other hand, $A_{V,\mathrm{depl}}$ is an average of the dust extinction in the warm neutral medium of the absorbing galaxies and would be more sensitive to gray dust. The presence of gray dust would result in $A_{V,\mathrm{depl}} > A_{V,\mathrm{ext}}$. Most of the $A_{V,\mathrm{ext}}$ measurements for GRB-DLAs are made whilst adopting an X-ray spectral slope (e.g., Heintz et al. 2019) and this makes them more robust in the presence of gray dust. In any case, we observe only a few systems with significant $A_{V,\mathrm{depl}} > A_{V,\mathrm{ext}}$, which possibly limits the effects of gray dust in this work.

The shape of the extinction curves depends on several properties, and can be steeper at lower metallicities (e.g., Shivaei et al. 2020), as is the case for GRB-DLAs. $A_{V,\mathrm{ext}}$ and $A_{V,\mathrm{depl}}$ may be probing different types of dust and different regions with lower or higher densities. The methods used to measure $A_{V,\mathrm{ext}}$ and $A_{V,\mathrm{depl}}$ are very different: $A_{V,\mathrm{ext}}$ represents a sum of the extinction integrated along the line of sight, including clumps of dense cold regions and intervening systems at lower z, while $A_{V,\mathrm{depl}}$ represents an average value in the warm neutral medium through galaxies. On the other hand, the composition of dust plays a role in dust extinction, because $A_{\rm V,ext}$ is very sensitive to C-rich dust, but constraining the depletion of C is challenging. For the calculation of $A_{\rm V,depl}$, we take C into account. However, only five Milky Way measurements are available (see Fig. B.2 of Paper I). These are based on only one weak transition (λ 2325 Å), because the allowed transitions at λ 1036 Å and λ 1335 Å are strongly saturated (Jenkins 2009). In Paper I we adopted the laboratory oscillator strength measurements with no additional correction for the oscillator strength of C.

In Paper I, using the depletion coefficients, we extrapolated the C depletion measured from a few Milky Way systems to the other environments where no measurements are available. This could mean that the depletion of C might be underestimated and might lead to a lower $A_{\rm V,depl}$. On the other hand, $A_{\rm V,ext}$ is estimated by also probing C grains, especially in the Milky Way, which has the strongest 2175 Å feature. This could partly explain the higher values of $A_{\rm V,ext}$ and the large discrepancy with $A_{\rm V,depl}$ for the cases where C is present, as it is for most of the targets in the Milky Way.

Moreover, the presence of C-rich dust confined in molecular clouds may explain the discrepancy between $A_{\rm V,depl}$ and $A_{\rm V,ext}$ in a few outliers in the Magellanic Clouds as well as in the Milky Way (see Fig. 7). The highly deviating points, namely Sk 143 (SMC) at $A_{\rm V,ext} = 0.97$ and Sk 672 (LMC) at $A_{\rm V,ext} = 0.76$, which are marked with green circles in Fig. 7, are moderately reddened stars and the lines of sight with the highest molecular fraction and CN absorption within the SMC and LMC sample (Cartledge et al. 2006; Welty et al. 2006). Also, Sk 143 is the only SMC line of sight known to exhibit a Milky Way-like extinction curve, with a 2175 Å extinction bump (Gordon et al. 2003; Welty & Crowther 2010). In the LMC, Sk 6619 fits a Milky Way-like extinction curve (Gordon et al. 2003) and is marked with a green circle point above the 1:1 line seen in Fig. 7.

The good agreement between the two extinction estimates for GRB-DLAs can be explained by the fact the two measurements may be probing dust with similar composition – because there may be less C-rich dust given the low metallicity – and in similar regions – because the GRB is expected to photo-dissociate the surrounding dense region (e.g., Ledoux et al. 2009), possibly leading to $A_{\rm V,ext}$ being more representative of the diffuse warm neutral medium in the host galaxy. In general, the measurements of $A_{\rm V,ext}$ in GRB afterglows are reliable (Watson et al. 2006; Zafar & Watson 2013; Perley et al. 2013; Heintz et al. 2019), because the intrinsic afterglow spectrum is known to be either a power law or a broken power law (e.g., Sari et al. 1998).

Overall, $A_{\rm V,depl}$ and $A_{\rm V,ext}$ do not measure dust in the same way or in the same regions. $A_{\rm V,depl}$ measures the average extinction along the line of sight, while only dusty clouds contribute to $A_{\rm V,ext}$ (i.e., the latter is not sensitive to the dust-free segments of the line of sight). The analysis of the depletion is mostly probing the warm neutral medium, and is less sensitive to the dense clumps of cold molecular gas, which may contain large fractions of C-rich dust. This is likely the cause of the discrepancy between $A_{\rm V,depl}$ and $A_{\rm V,ext}$ observed in the Milky Way and a few lines of sight in the Magellanic Clouds.

5. Conclusions

In this study, we measured the dust-to-metal (DTM), dust-to-gas (DTG) ratios, dust extinction from depletion $A_{\rm V,depl}$, and the fraction of dust mass contributed by element X ($f_{\rm M_X}$) from the dust depletion of all the elements that contribute to dust. We did this for systems in different environments, namely QSO-DLAs, GRB-DLAs, the LMC, the SMC, and the Milky Way. We study the DTM, DTG, and $A_{\rm V,depl}$ evolution with the dust-corrected metallicity and the dust tracer [Zn/Fe]. The evolution of the DTM and DTG with metallicity provides clues as to the dominant mechanisms of dust production. We find that the DTM and DTG ratios increase with metallicity and with [Zn/Fe], which suggests that the dominant mechanism for dust production in the metallicity range ($-2 \leq$ [M/H]$_{\rm tot} \leq 0.5$) and redshift range ($0.6 < z < 6.3$) that we study is grain growth in the ISM. Our data are in very good agreement with the dust production and evolution model from Mattsson (2020). The comparison of our data with this latter model indicates that the stellar dust yield is only 1% of the metals yield, which suggests that the net amount of dust that the overall stellar population produces is about ten times less than what was previously estimated. However, we note that this could be an effect of observational bias, because our data probe sightlines of warm diffuse gas and, as a result, might be missing some dust production contributions from stellar sources. We investigated the cosmic metallicity evolution of the neutral gas and find a declining evolution with increasing redshift, which is probed both with QSO-DLAs and GRB-DLAs in a similar way.

The main elements that contribute to dust are, in order of mass abundance, O, Fe, Si, Mg, C, S, Ni, and Al for different environments and with similar percentages overall. Si, Mg, and C make similar contributions to dust – by mass – in all the environments studied here and vary with the amount of dust in each system, as traced by [Zn/Fe]. O and Fe have the highest fractions among all studied elements and show opposite trends with [Zn/Fe]; that is, O (and C) increases, while Fe decreases with [Zn/Fe]. This opposite evolution may be due to the greater availability of Fe in systems with lower levels of depletion. In the low-dust regime ([Zn/Fe] < 0.3), we find that the amount of O in dust is about three times that of Si. This suggests the presence of pyroxenes as the main dust species.

We calculated the dust-to-metal ratio in terms of column density (DTM$_{\rm N}$) in order to estimate the dust extinction using dust depletion ($A_{\rm V,depl}$). The dust extinction $A_{\rm V,depl}$ increases with metallicity and with [Zn/Fe]. At any given metallicity, we find lower values of $A_{\rm V,depl}$ for QSO-DLAs than for GRB-DLAs, the Milky Way, and the Magellanic Clouds. This suggest that it is not only metallicity that is a determinant factor facilitating the growth of dust in the ISM, but also the presence of dense cold gas at high pressure (such as in galaxy disks).

We compared the dust extinction estimated from depletion ($A_{\rm V,depl}$) with that estimated from the SED or from the reddening ($A_{\rm V,ext}$). We find an overall good agreement between $A_{\rm V,depl}$ and $A_{\rm V,ext}$. However, we find that $A_{\rm V,depl}$ is much lower than $A_{\rm V,ext}$ in the Milky Way, and find that this is also true in a few systems in the SMC and LMC. In all these cases, the systems show a 2175 Å bump in their extinction curves. The likely cause of the discrepancy is the presence of C-rich dust in clumps of dense cold gas, such as molecular clouds, which are not probed by the depletion measurements. Overall, $A_{\rm V,depl}$ and $A_{\rm V,ext}$ do not measure the amount of dust in the same way and in the same regions, with $A_{\rm V,depl}$ measuring an average extinction along the line of sight and $A_{\rm V,ext}$ being sensitive to dust-rich clouds. Nevertheless, in this work we refine the measurements of $A_{\rm V,depl}$ and find these to be more consistent with $A_{\rm V,ext}$. The discrepancies that remain are probably related to the presence of C-rich dust in clumps of cold dense gas.

Acknowledgements. We thank the anonymous referee for the useful and constructive comments that improved this manuscript. C.K., A.D.C. and T.R.H. acknowledge support by the Swiss National Science Foundation under grant 185692. K.E.H. acknowledges support from the Carlsberg Foundation Reintegration Fellowship Grant CF21-0103. A.C.A. would like to acknowledge support by the Carlsberg Foundation. The Cosmic Dawn Center (DAWN) is funded by the Danish National Research Foundation under grant no. 140. This research has made use of NASA's Astrophysics Data System.

References

Asplund, M., Amarsi, A. M., & Grevesse, N. 2021, A&A, 653, A141
Berg, T. A. M., Ellison, S. L., Prochaska, J. X., Venn, K. A., & Dessauges-Zavadsky, M. 2015, MNRAS, 452, 4326
Blitz, L., & Rosolowsky, E. 2006, ApJ, 650, 933
Bocchio, M., Jones, A. P., & Slavin, J. D. 2014, A&A, 570, A32
Bolmer, J., Ledoux, C., Wiseman, P., et al. 2019, A&A, 623, A43
Calzetti, D., Bohlin, R. C., Gordon, K. D., Witt, A. N., & Bianchi, L. 1995, ApJ, 446, L97
Cartledge, S. I. B., Lauroesch, J. T., Meyer, D. M., & Sofia, U. J. 2006, ApJ, 641, 327
De Cia, A., Ledoux, C., Savaglio, S., Schady, P., & Vreeswijk, P. M. 2013, A&A, 560, A88
De Cia, A., Ledoux, C., Mattsson, L., et al. 2016, A&A, 596, A97
De Cia, A., Ledoux, C., Petitjean, P., & Savaglio, S. 2018, A&A, 611, A76
De Cia, A., Jenkins, E. B., Fox, A. J., et al. 2021, Nature, 597, 206
D'Elia, V., Campana, S., Covino, S., et al. 2011, MNRAS, 418, 680
De Vis, P., Gomez, H. L., Schofield, S. P., et al. 2017, MNRAS, 471, 1743
Draine, B. T. 2003, ARA&A, 41, 241
Draine, B. T., & Li, A. 2007, ApJ, 657, 810
Dunne, L., Eales, S., Ivison, R., Morgan, H., & Edmunds, M. 2003, Nature, 424, 285
Dwek, E. 2016, ApJ, 825, 136
Dwek, E., Foster, S. M., & Vancura, O. 1996, ApJ, 457, 244
Elíasdóttir, Á., Fynbo, J. P. U., Hjorth, J., et al. 2009, ApJ, 697, 1725
Feldmann, R. 2015, MNRAS, 449, 3274
Field, G. B. 1974, ApJ, 187, 453
Friis, M., De Cia, A., Krühler, T., et al. 2015, MNRAS, 451, 167
Fynbo, J. P. U., Prochaska, J. X., Sommer-Larsen, J., Dessauges-Zavadsky, M., & Møller, P. 2008, ApJ, 683, 321
Gail, H. P., Zhukovska, S. V., Hoppe, P., & Trieloff, M. 2009, ApJ, 698, 1136
Galliano, F., Dwek, E., & Chanial, P. 2008, ApJ, 672, 214
Galliano, F., Galametz, M., & Jones, A. P. 2018, ARA&A, 56, 673
Gordon, K. D., & Clayton, G. C. 1998, ApJ, 500, 816
Gordon, K. D., Clayton, G. C., Misselt, K. A., Landolt, A. U., & Wolff, M. J. 2003, ApJ, 594, 279
Gustafsson, B. 2022, Universe, 8, 409
Gustafsson, B., Karlsson, T., Olsson, E., Edvardsson, B., & Ryde, N. 1999, A&A, 342, 426
Heintz, K. E., Fynbo, J. P. U., Møller, P., et al. 2016, A&A, 595, A13
Heintz, K. E., Ledoux, C., Fynbo, J. P. U., et al. 2019, A&A, 621, A20
Heintz, K. E., De Cia, A., Thöne, C. C., et al. 2023, A&A, 679, A91
Hoffman, J., & Draine, B. T. 2016, ApJ, 817, 139
Höfner, S., & Olofsson, H. 2018, A&ARv, 26, 1
Hollenbach, D., & McKee, C. F. 1979, ApJS, 41, 555
Hollenbach, D., & Salpeter, E. E. 1971, ApJ, 163, 155
Issa, M. R., MacLaren, I., & Wolfendale, A. W. 1990, A&A, 236, 237
Jenkins, E. B. 2009, ApJ, 700, 1299
Jenkins, E. B. 2014, ArXiv e-prints [arXiv:`1402.4765`]
Jenkins, E. B., & Wallerstein, G. 2017, ApJ, 838, 85
Jones, A. P., Tielens, A. G. G. M., & Hollenbach, D. J. 1996, ApJ, 469, 740
Konstantopoulou, C., De Cia, A., Krogager, J.-K., et al. 2022, A&A, 666, A12
Konstantopoulou, De Cia, Annalisa, Krogager, Jens-Kristian, et al. 2023, A&A, 674, C1
Krogager, J. K., Fynbo, J. P. U., Heintz, K. E., et al. 2016, ApJ, 832, 49
Krogager, J.-K., Fynbo, J. P. U., Møller, P., et al. 2019, MNRAS, 486, 4377
Krogager, J. K., Leighly, K. M., Fynbo, J. P. U., et al. 2023, The Messenger, 190, 38
Ledoux, C., Vreeswijk, P. M., Smette, A., et al. 2009, A&A, 506, 661
Li, Q., Narayanan, D., & Davé, R. 2019, MNRAS, 490, 1425
Lisenfeld, U., & Ferrara, A. 1998, ApJ, 496, 145
Lodders, K., Palme, H., & Gail, H. P. 2009, in Landolt-Börnstein - Group VI Astronomy and Astrophysics 4B, ed. J. E. Trümper, 4.4 (Springer-Verlag), 560
Maiolino, R., & Mannucci, F. 2019, A&ARv, 27, 3
Mathis, J. S. 1994, ApJ, 422, 176
Mathis, J. S., Rumpl, W., & Nordsieck, K. H. 1977, ApJ, 217, 425
Matsuura, M., Dwek, E., Barlow, M. J., et al. 2015, ApJ, 800, 50
Mattsson, L. 2010, A&A, 515, A68
Mattsson, L. 2020, MNRAS, 499, 6035
Mattsson, L., Andersen, A. C., & Munkhammar, J. D. 2012, MNRAS, 423, 26
Mattsson, L., De Cia, A., Andersen, A. C., & Zafar, T. 2014, MNRAS, 440, 1562
Mattsson, L., De Cia, A., Andersen, A. C., & Petitjean, P. 2019, A&A, 624, A103
Nagao, T., Maeda, K., & Yamanaka, M. 2018, MNRAS, 476, 4806
Noterdaeme, P., Ledoux, C., Petitjean, P., & Srianand, R. 2008, A&A, 481, 327
Pei, Y. C. 1992, ApJ, 395, 130
Perley, D. A., Levan, A. J., Tanvir, N. R., et al. 2013, ApJ, 778, 128
Péroux, C., & Howk, J. C. 2020, ARA&A, 58, 363
Péroux, C., De Cia, A., & Howk, J. C. 2023, MNRAS, 522, 4852
Phillips, A. P., Gondhalekar, P. M., & Pettini, M. 1982, MNRAS, 200, 687
Piranomonte, S., Ward, P. A., Fiore, F., et al. 2008, A&A, 492, 775
Planck Collaboration VI 2020, A&A, 641, A6
Prochaska, J. X., Chen, H.-W., Dessauges-Zavadsky, M., & Bloom, J. S. 2007, ApJ, 666, 267
Rémy-Ruyer, A., Madden, S. C., Galliano, F., et al. 2014, A&A, 563, A31
Roman-Duval, J., Jenkins, E. B., Tchernyshyov, K., et al. 2021, ApJ, 910, 95
Roman-Duval, J., Jenkins, E. B., Tchernyshyov, K., et al. 2022a, ApJ, 928, 90
Roman-Duval, J., Jenkins, E. B., Tchernyshyov, K., et al. 2022b, ApJ, 935, 105
Saccardi, A., Vergani, S. D., De Cia, A., et al. 2023, A&A, 671, A84
Sandstrom, K. M., Bolatto, A. D., Draine, B. T., Bot, C., & Stanimirović, S. 2010, ApJ, 715, 701
Sari, R., Piran, T., & Narayan, R. 1998, ApJ, 497, L17
Savage, B. D., & Sembach, K. R. 1996, ARA&A, 34, 279
Savaglio, S., & Fall, S. M. 2004, ApJ, 614, 293
Savaglio, S., Fall, S. M., & Fiore, F. 2003, ApJ, 585, 638
Schady, P., Dwelly, T., Page, M. J., et al. 2012, A&A, 537, A15
Shin, M.-S., Berger, E., Penprase, B. E., et al. 2006, ArXiv e-prints [arXiv:`astro-ph/0608327`]
Shivaei, I., Darvish, B., Sattari, Z., et al. 2020, ApJ, 903, L28
Shivaei, I., Boogaard, L., Díaz-Santos, T., et al. 2022, MNRAS, 514, 1886
Slavin, J. D., Dwek, E., & Jones, A. P. 2015, ApJ, 803, 7
Tchernyshyov, K., Meixner, M., Seale, J., et al. 2015, ApJ, 811, 78
Valiante, R., Schneider, R., Bianchi, S., & Andersen, A. C. 2009, MNRAS, 397, 1661
Watson, D. 2011, A&A, 533, A16
Watson, D., Fynbo, J. P. U., Ledoux, C., et al. 2006, ApJ, 652, 1011
Welty, D. E., & Crowther, P. A. 2010, MNRAS, 404, 1321
Welty, D. E., Federman, S. R., Gredel, R., Thorburn, J. A., & Lambert, D. L. 2006, ApJS, 165, 138
Wiseman, P., Schady, P., Bolmer, J., et al. 2017, A&A, 599, A24
Witt, A. N., & Gordon, K. D. 2000, ApJ, 528, 799
Zafar, T., & Møller, P. 2019, MNRAS, 482, 2731
Zafar, T., & Watson, D. 2013, A&A, 560, A26
Zafar, T., Watson, D., Fynbo, J. P. U., et al. 2011, A&A, 532, A143
Zafar, T., Watson, D., Elíasdóttir, Á., et al. 2012, ApJ, 753, 82
Zhukovska, S., Gail, H. P., & Trieloff, M. 2008, A&A, 479, 453

Appendix A: Additional figures

Here we present additional figures for the relation between the DTM by mass and the DTM by column density ($\mathrm{DTM_N}$) and for the dust composition $f_{\mathrm{M_X}}$ with respect to [Zn/Fe] for all the elements that contribute to dust with $f_{\mathrm{M_X}} > 1\%$; namely O, S, Si, Mg, Fe, Ni, Al, and C. In the dust composition figures, we show the targets that have dust-depletion measurements with filled symbols and the ones whose dust depletion is calculated from the coefficients listed in Table 1 with empty symbols. These are shown for each environment: QSO-DLAs and GRB-DLAs, the Milky Way, the LMC, and the SMC.

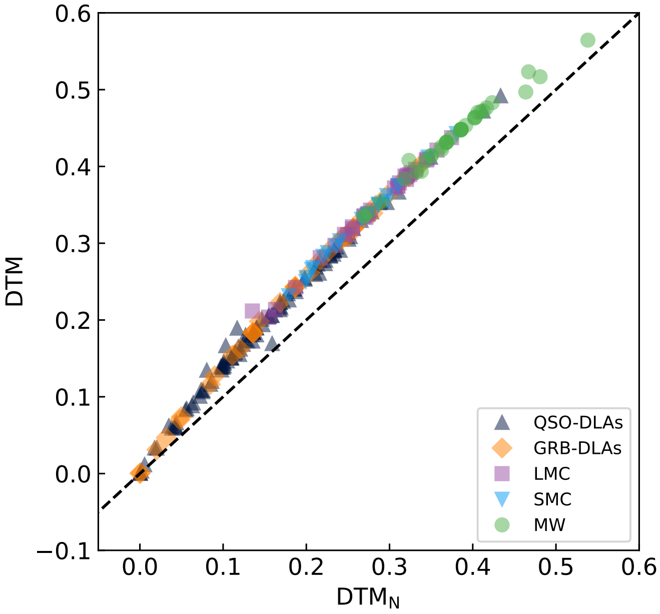

Fig. A.1: Relation between the DTM calculated in terms of mass and the DTM calculated in terms of column density ($\mathrm{DTM_N}$) for QSO-DLAs and GRB-DLAs, LMC, SMC, and the Milky Way. The dashed line is the 1:1 line of equality. DTM is on average ∼ 0.05 times higher than $\mathrm{DTM_N}$.

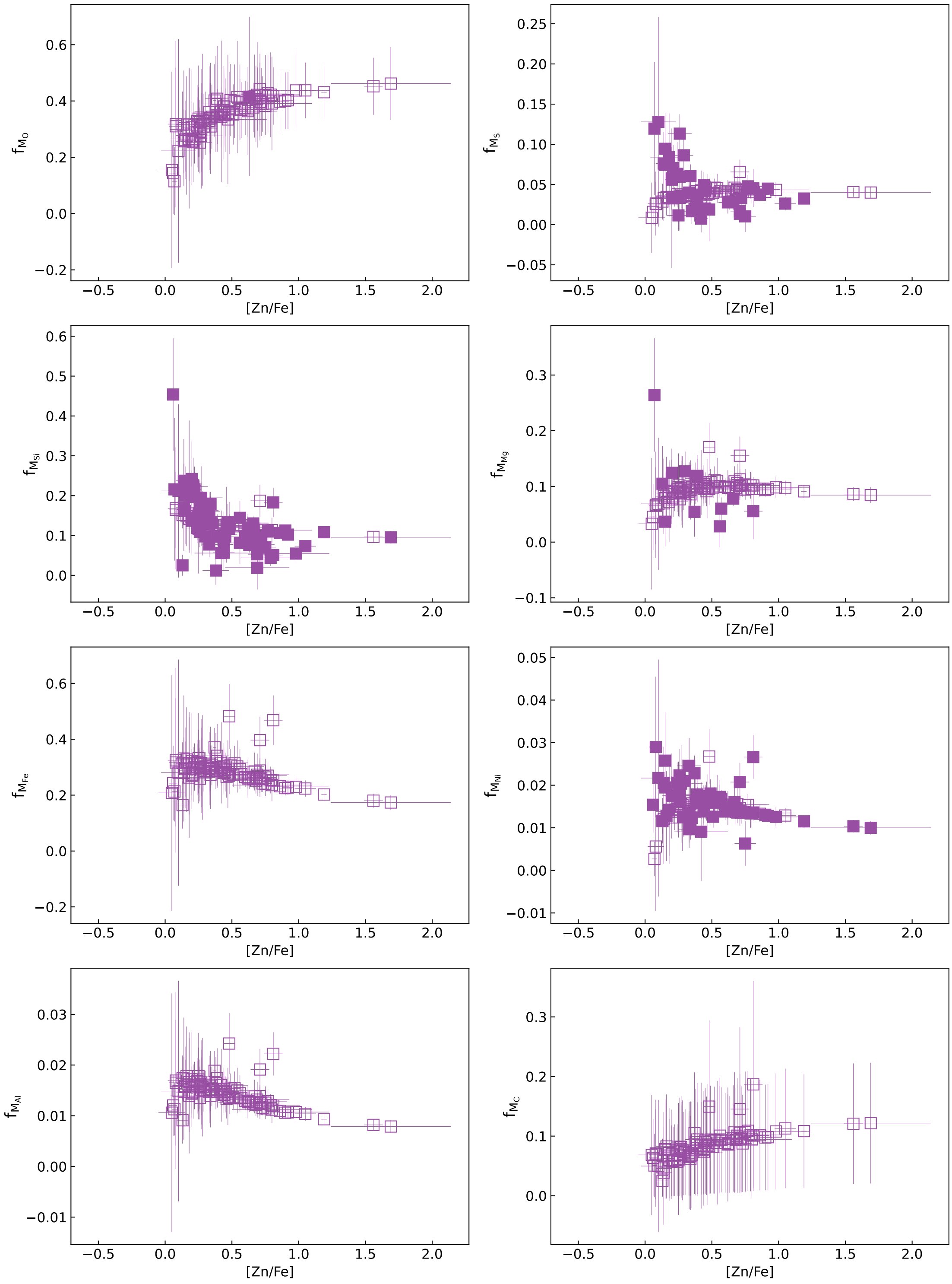

Fig. A.2: Fraction of dust mass contributed by element X, f_{M_X} as a function of the dust tracer [Zn/Fe] for QSO-DLAs. The filled squares indicate the targets that have a dust depletion measurement and the empty symbols indicate the targets whose dust depletion is calculated from the coefficients listed in Table 1.

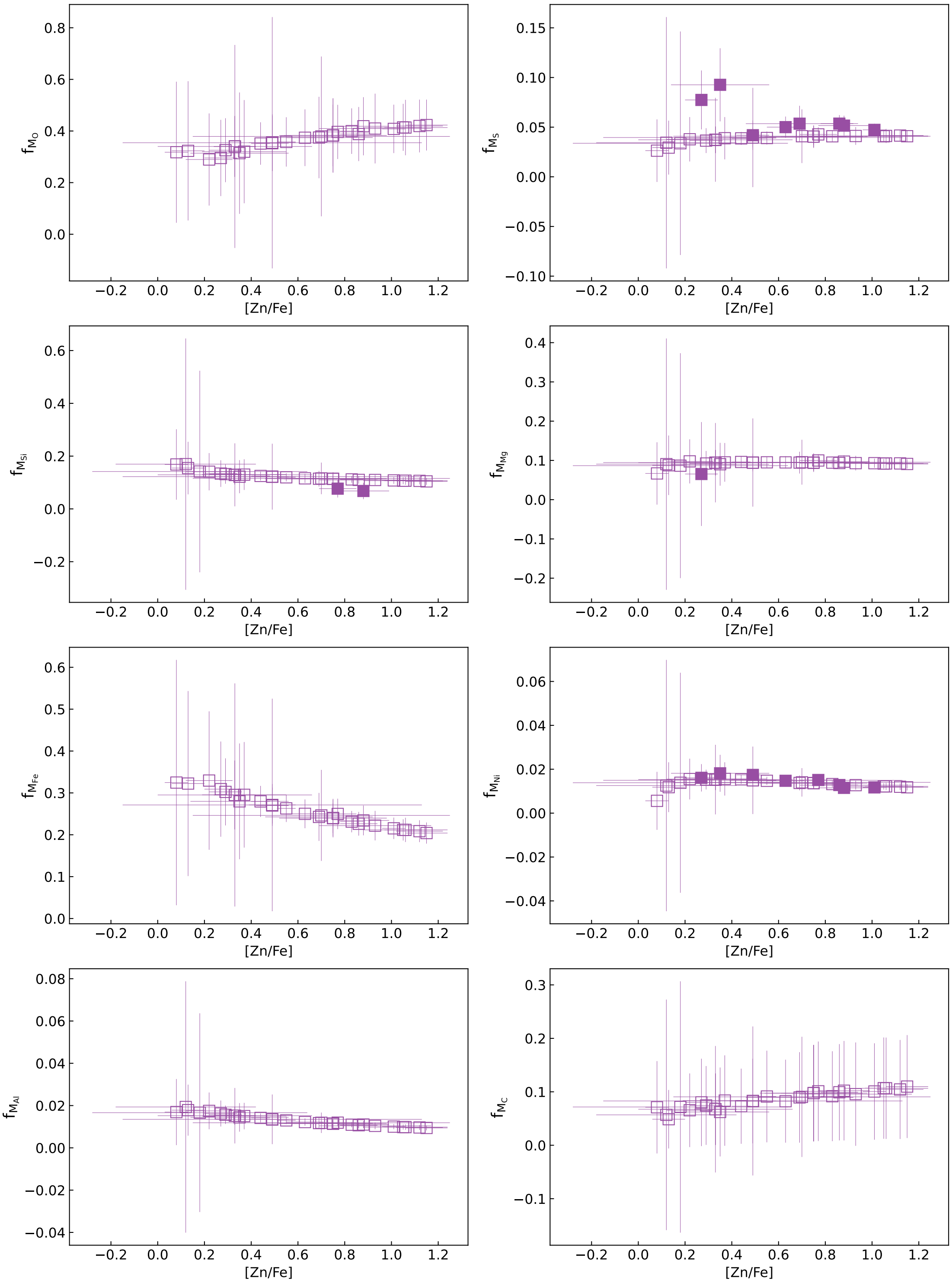

Fig. A.3: Fraction of dust mass contributed by element X, f_{M_X} as a function of the dust tracer [Zn/Fe] for GRB-DLAs.

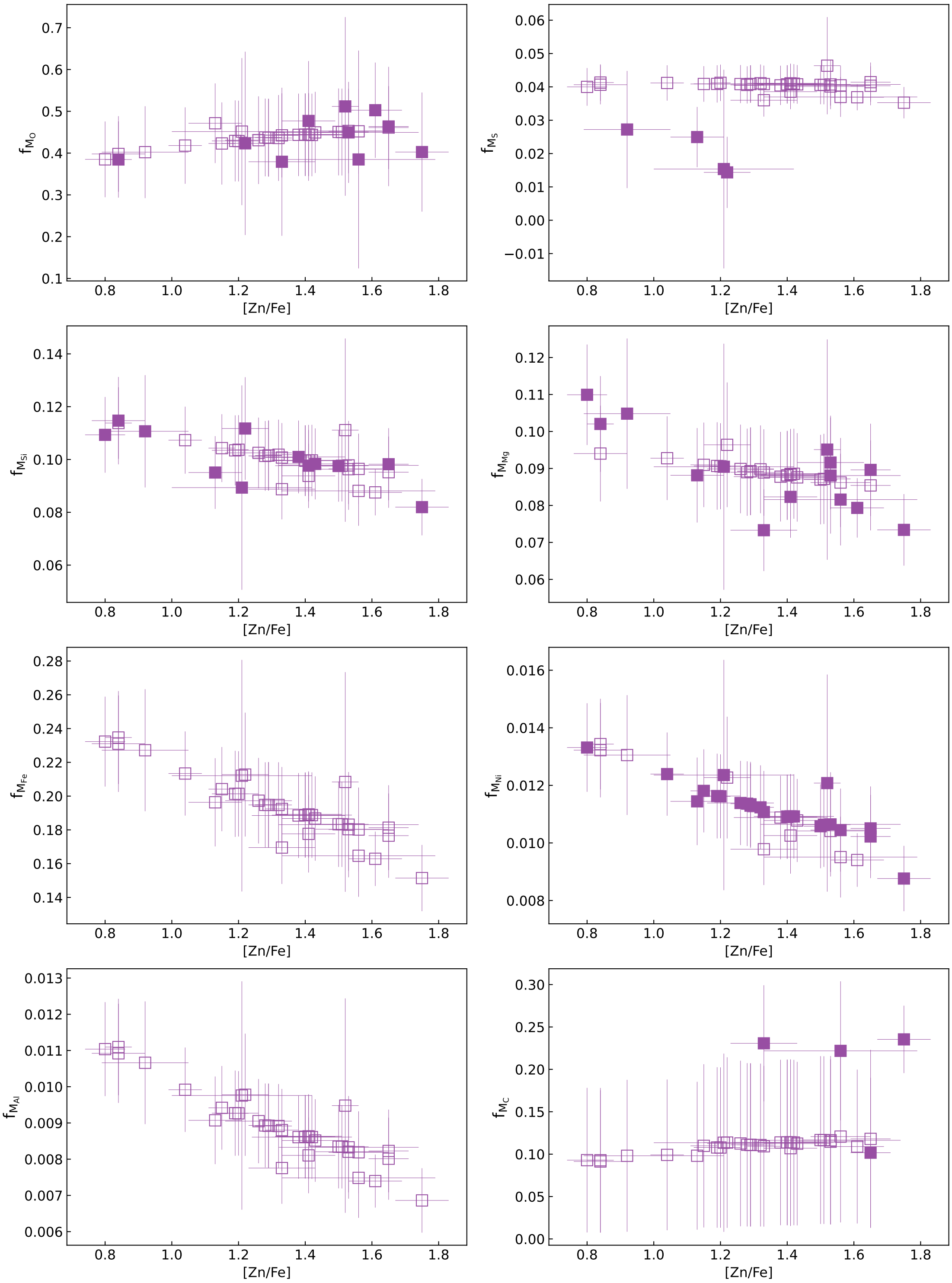

Fig. A.4: Fraction of dust mass contributed by element X, f_{M_X} as a function of the dust tracer [Zn/Fe] for the Milky Way.

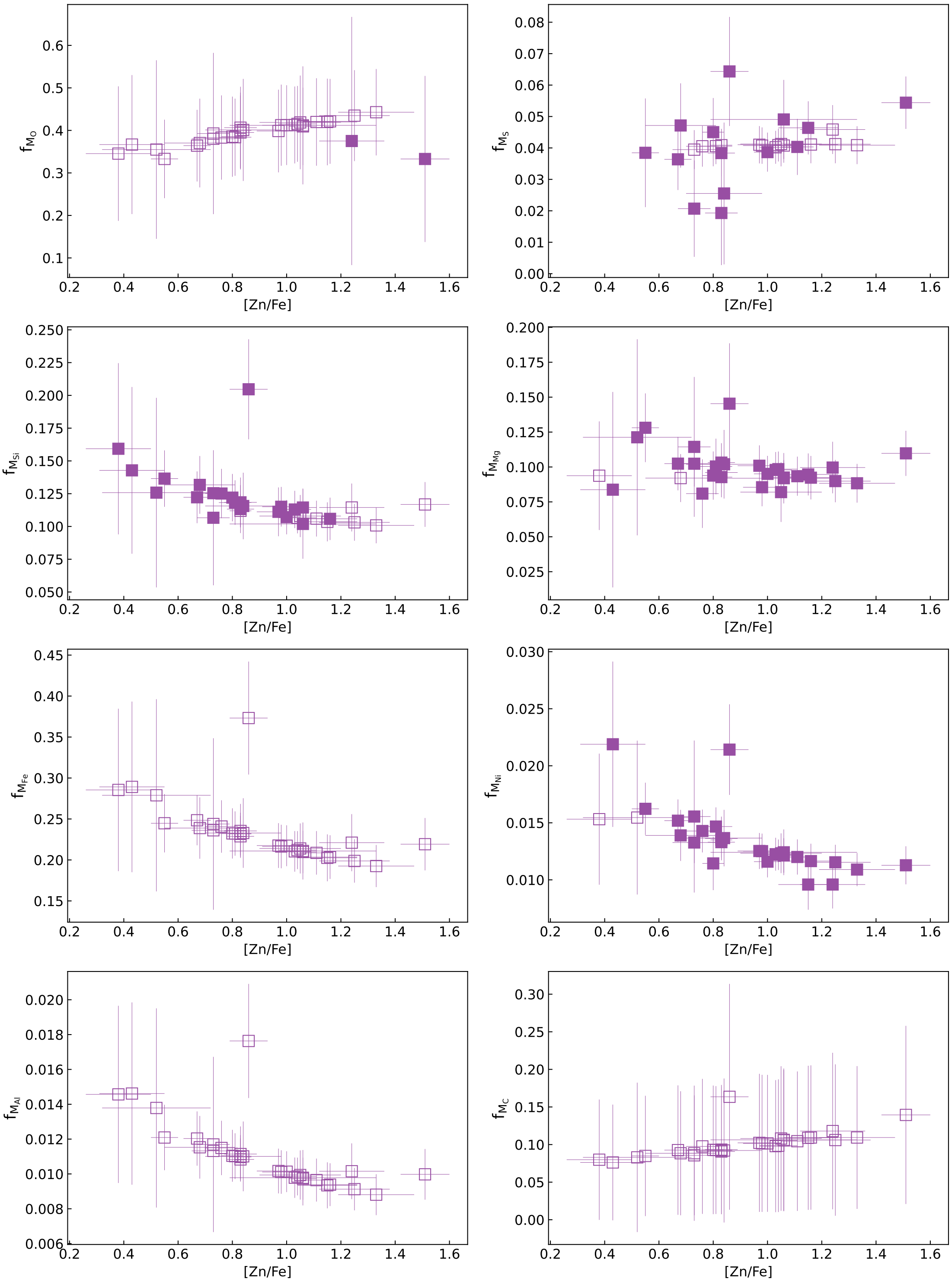

Fig. A.5: Fraction of dust mass contributed by element X, f_{M_X} as a function of the dust tracer [Zn/Fe] for the LMC.

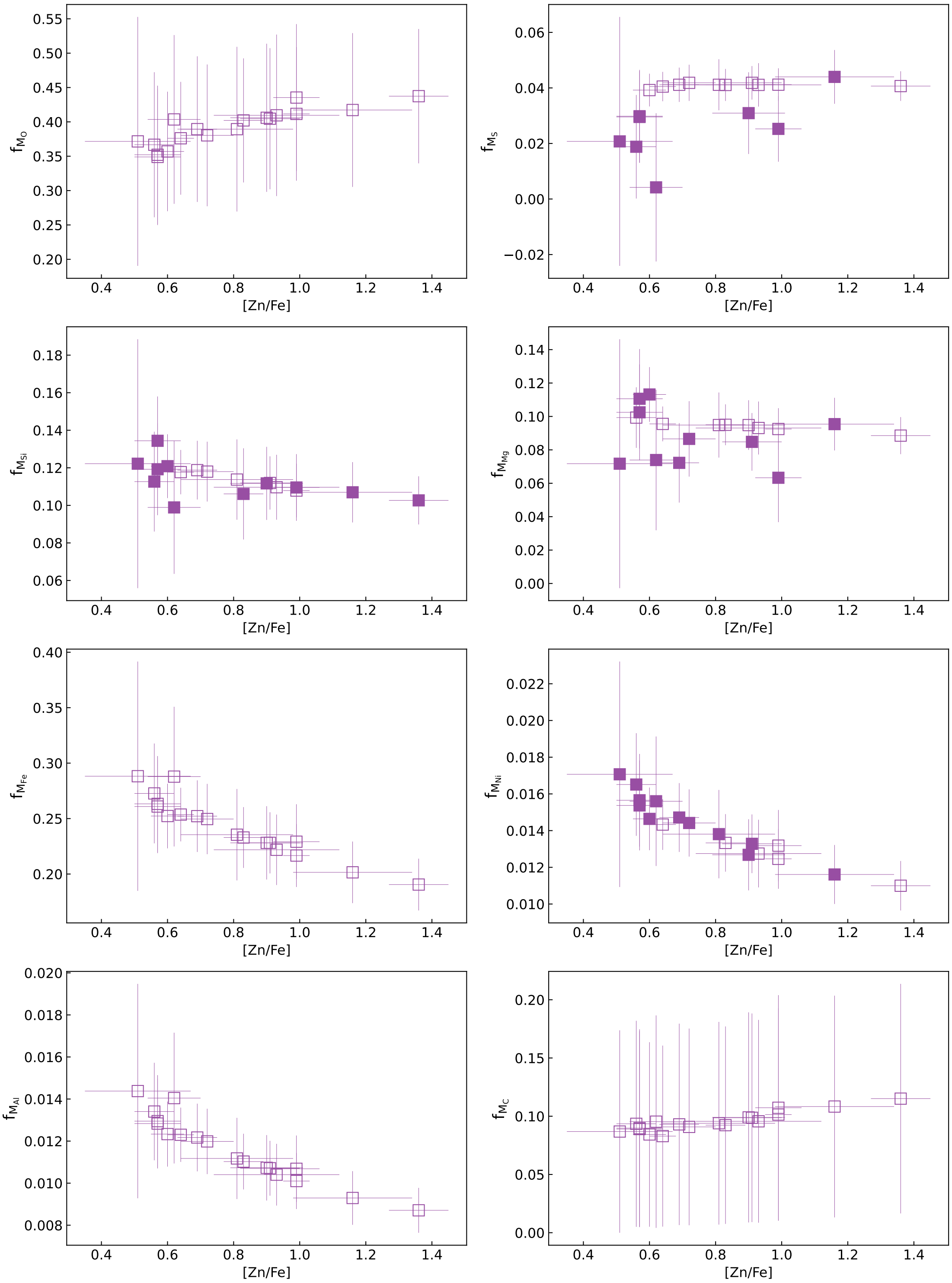

Fig. A.6: Fraction of dust mass contributed by element X, f_{M_X} as a function of the dust tracer [Zn/Fe] for the SMC.

Appendix B: Dust properties of the data sample

Here we present the tables of the dust properties for QSO-DLAs and GRB-DLAs, the Milky Way, the LMC and the SMC. We include the redshift $z_{\rm abs}$, the column densities of H I and H II, the dust tracer [Zn/Fe], the DTM and DTG in terms of mass, the DTM in terms of column density ($\rm DTM_N$), the dust extinction estimated from the dust depletion $A_{\rm V,depl}$, and the total dust-corrected metallicity $\rm [M/H]_{tot}$. We note that the DTM in terms of column density ($\rm DTM_N$) is not normalized by the Galactic DTM. We also report the references of the data samples.

Table B.1: QSO-DLAs dust properties

QSO	z_{abs}	log N(H I)	log N(H 2)	[Zn/Fe]	DTM	DTG	$\mathrm{DTM_N}$	$A_{V,\mathrm{depl}}$	$[\mathrm{M/H}]_{\mathrm{tot}}$	Ref
B0105-008	1.371	21.70±0.15	...	0.08±0.05	0.06±0.02	4.00e-05±2.00e-05	0.04±0.01	0.01±0.01	-1.35±0.17	*,2,3
B2314-409	1.857	20.90±0.10	...	0.18±0.14	0.14±0.04	2.30e-04±1.20e-04	0.10±0.03	0.01±0.01	-0.92±0.19	*,2,3
B2355-106	1.173	21.00±0.10	...	0.42±0.20	0.19±0.05	5.10e-04±3.00e-04	0.15±0.05	0.04±0.02	-0.72±0.23	*,2,3
BRI1013+0035	3.104	21.10±0.10	...	0.90±0.05	0.35±0.04	3.82e-03±1.24e-03	0.29±0.06	0.36±0.15	-0.11±0.13	*,2,3
FJ0812+32	2.626	21.35±0.10	...	0.81±0.07	0.17±0.14	6.10e-04±5.40e-04	0.10±0.15	0.08±0.12	-0.58±0.14	*,2,3
FJ0812+32	2.067	21.00±0.10	...	0.06±0.03	0.07±0.02	4.00e-05±1.00e-05	0.04±0.01	...	-1.37±0.13	*,2,3
FJ2334-0908	3.057	20.48±0.05	...	0.48±0.04	0.13±0.15	2.90e-04±3.20e-04	0.08±0.16	0.003±0.001	-0.81±0.09	*,2,3
HE0515-4414	1.150	20.45±0.15	...	0.54±0.20	0.23±0.05	5.10e-04±3.20e-04	0.18±0.05	0.01±0.01	-0.79±0.26	*,2,3
HE1104-1805	1.662	20.85±0.01	...	0.46±0.02	0.39±0.10	7.80e-04±2.30e-04	0.35±0.10	0.05±0.02	-0.84±0.07	*,2,3
J0000+0048	2.525	21.07±0.10	...	1.69±0.45	0.49±0.07	5.43e-02±6.06e-02	0.43±0.09	...	0.90±0.48	*,2,3
J0008-0958	1.768	20.85±0.15	...	0.44±0.07	0.21±0.03	...	0.16±0.03	...	...	*,2,3
J0058+0115	2.010	21.10±0.15	...	0.51±0.07	0.24±0.03	8.50e-04±3.70e-04	0.19±0.04	0.08±0.04	-0.60±0.18	*,2,3
J0256+0110	0.725	20.70±0.16	...	0.80±0.30	0.33±0.06	6.18e-03±5.38e-03	0.27±0.07	0.23±0.22	0.13±0.37	*,2,3
J0927+1543	1.731	...	...	0.98±0.25	0.35±0.06	...	0.30±0.07	...	...	*,2,3
J1049-0110	1.658	20.31±0.15	...	0.71±0.07	0.26±0.04	9.32e-03±4.11e-03	0.22±0.05	0.14±0.08	0.41±0.18	*,2,3
J1056+1208	1.610	21.45±0.15	...	0.69±0.07	0.28±0.04	3.20e-03±1.39e-03	0.23±0.05	0.67±0.39	-0.09±0.18	*,2,3
J1107+0048	0.740	21.00±0.05	...	0.28±0.105	0.16±0.03	8.00e-04±3.50e-04	0.12±0.03	0.05±0.03	-0.45±0.17	*,2,3
J1135-0010	2.207	22.05±0.10	...	0.60±0.04	0.27±0.03	5.20e-04±1.70e-04	0.21±0.04	0.42±0.18	-0.86±0.13	*,2,3
J1142+0701	1.841	21.50±0.15	...	0.56±0.07	0.25±0.03	7.90e-04±3.40e-04	0.20±0.04	0.18±0.10	-0.65±0.18	*,2,3
J1155+0530	3.326	21.05±0.10	...	0.26±0.09	0.18±0.02	5.20e-04±1.90e-04	0.13±0.03	0.04±0.02	-0.68±0.15	*,2,3
J1200+4015	3.220	20.65±0.15	...	0.29±0.07	0.17±0.02	1.22e-03±5.30e-04	0.13±0.03	0.04±0.02	-0.30±0.18	*,2,3
J1211+0833	2.117	21.00±0.20	...	1.56±0.07	0.47±0.06	1.73e-02±9.02e-03	0.41±0.08	1.38±0.98	0.42±0.22	*,2,3
J1237+0647	2.690	20.00±0.15	...	1.19±0.02	0.41±0.05	3.37e-02±1.38e-02	0.35±0.07	0.26±0.15	0.77±0.17	*,2,3
J1240+1455	3.108	21.30±0.20	...	1.05±0.08	0.37±0.05	9.90e-04±5.40e-04	0.31±0.06	0.15±0.11	-0.71±0.23	*,2,3
J1310+5424	1.801	21.45±0.15	...	0.67±0.07	0.26±0.05	1.85e-03±8.30e-04	0.21±0.05	0.39±0.23	-0.29±0.18	*,2,3
J1313+1441	1.795	...	...	0.49±0.07	0.21±0.03	...	0.17±0.04	...	...	*,2,3
J1417+4132	1.951	21.45±0.25	...	0.71±0.07	0.19±0.19	...	0.12±0.21	...	...	*,2,3
J1431+3952	0.602	21.20±0.10	...	0.62±0.22	0.28±0.05	9.90e-04±5.90e-04	0.22±0.05	0.11±0.08	-0.59±0.25	*,2,3
J1454+0941	1.788	20.50±0.15	...	0.44±0.13	0.21±0.03	1.65e-03±8.40e-04	0.16±0.04	0.04±0.02	-0.24±0.21	*,2,3
J1541+3153	2.444	20.95±0.10	...	0.27±0.16	0.16±0.03	8.00e-05±4.00e-05	0.12±0.03	...	-1.45±0.20	*,2,3
J1552+4910	1.960	...	...	0.20±0.07	0.12±0.03	6.00e-05±2.00e-05	0.09±0.02	...	-1.46±0.13	*,2,3
J1604+3951	3.163	21.75±0.20	...	0.39±0.07	0.20±0.02	2.10e-04±1.10e-04	0.15±0.03	0.08±0.06	-1.12±0.22	*,2,3
J1623+0718	1.336	21.35±0.10	...	0.38±0.10	0.18±0.03	3.00e-04±1.20e-04	0.14±0.03	0.05±0.02	-0.93±0.16	*,2,3
J2328+0022	0.652	20.32±0.07	...	0.34±0.15	0.18±0.03	1.04e-03±4.70e-04	0.14±0.04	0.01±0.01	-0.39±0.18	*,2,3
J2340-00	2.054	20.35±0.15	...	0.39±0.09	0.17±0.03	1.51e-03±7.20e-04	0.14±0.04	0.02±0.01	-0.20±0.19	*,2,3
PSS1253-0228	2.783	21.85±0.20	...	0.16±0.08	0.10±0.02	3.00e-05±2.00e-05	0.07±0.02	0.01±0.01	-1.64±0.23	*,2,3
PSSJ2344+0342	3.220	21.25±0.08	...	-0.08±0.34	0.0011±0.120	3.00e-07±4.00e-05	0.001 ±0.08	...	-1.65±0.35	*,2,3
Q0000-263	3.390	21.40±0.08	...	-0.11±0.06	0.003±0.16	3.00e-07±2.00e-05	0.003±0.16	...	-2.14±0.11	*,1,3
Q0010-002	2.025	20.95±0.10	...	-0.25±0.06	0.0005±0.030	2.00e-07±1.00e-05	0.001±0.03	...	-1.49±0.13	*,1,3
Q0013-004	1.973	20.83±0.05	18.86±1.14	0.75±0.01	0.32±0.04	1.77e-03±4.60e-04	0.26±0.05	0.09±0.03	-0.40±0.10	*,1,3
Q0027-1836	2.402	21.75±0.10	17.30±0.07	0.56±0.03	0.24±0.03	1.30e-04±4.00e-05	0.19±0.04	0.05±0.02	-1.41±0.13	*,2,3
Q0058-292	2.671	21.10±0.10	...	0.24±0.03	0.14±0.01	6.00e-05±2.00e-05	0.10±0.02	0.01±0.001	-1.48±0.11	*,1,3
Q0100+130	2.309	21.35±0.08	...	0.13±0.01	0.09±0.01	3.00e-05±1.00e-05	0.06±0.01	...	-1.62±0.11	*,1,3
Q0102-190a	2.370	21.00±0.08	...	0.01±0.08	0.01±0.03	...	0.01±0.02	...	...	*,1,3
Q0149+33	2.141	20.50±0.10	...	0.05±0.10	0.06±0.03	2.00e-05±1.00e-05	0.04±0.02	...	-1.59±0.16	*,2,3
Q0201+365	2.463	20.38±0.05	...	0.20±0.05	0.14±0.02	1.67e-03±4.70e-04	0.10±0.02	0.03±0.01	-0.07±0.11	*,2,3
Q0216+080a	1.769	20.30±0.10	...	0.24±0.06	0.15±0.02	1.90e-04±7.00e-05	0.10±0.02	...	-1.02±0.13	*,1,3
Q0216+080b	2.293	20.50±0.10	...	0.33±0.05	0.17±0.02	5.90e-04±2.20e-04	0.13±0.03	0.01±0.01	-0.61±0.15	*,1,3
Q0302-223	1.009	20.36±0.11	...	0.52±0.08	0.22±0.03	1.31e-03±4.90e-04	0.17±0.04	0.02±0.01	-0.36±0.15	*,2,3
Q0347-383	3.025	20.73±0.05	14.53±0.06	0.63±0.05	0.28±0.08	3.10e-04±1.50e-04	0.22±0.09	0.01±0.01	-1.10 ±0.18	*,1,3
Q0405-443a	1.913	20.80±0.10	...	0.02±0.04	0.03±0.02	4.00e-05±2.00e-05	0.02±0.01	...	-1.08±0.12	*,1,3
Q0405-443b	2.550	21.15±0.15	...	0.15±0.04	0.11±0.02	5.00e-05±2.00e-05	0.08±0.02	...	-1.46±0.18	*,1,3
Q0405-443c	2.595	21.05±0.10	18.14±0.07	0.26±0.01	0.15±0.02	1.50e-04±4.00e-05	0.11±0.02	0.01±0.001	-1.14±0.12	*,1,3
Q0449-1645	1.007	20.98±0.07	...	0.27±0.07	0.16±0.02	2.90e-04±9.00e-05	0.11±0.03	0.02±0.01	-0.88±0.12	*,2,3
Q0458-020	2.040	21.70±0.10	...	0.57±0.04	0.25±0.03	2.50e-04±1.00e-04	0.20±0.04	0.09±0.04	-1.15±0.16	*,1,3
Q0528-250a	2.141	20.98±0.05	...	0.25±0.04	0.14±0.02	9.00e-05±2.00e-05	0.10±0.02	0.010±0.001	-1.35±0.08	*,1,3
Q0528-250b	2.811	21.35±0.07	18.22±0.11	0.37±0.01	0.16±0.02	2.70e-04±9.00e-05	0.12±0.03	0.04±0.02	-0.90±0.12	*,1,3
Q0551-366	1.962	20.70±0.08	17.42±0.14	0.71±0.04	0.29±0.04	2.26e-03±6.50e-04	0.23±0.05	0.08±0.03	-0.25±0.11	*,1,3
Q0642-5038	2.659	20.95±0.08	...	0.22±0.05	0.14±0.02	3.00e-05±1.00e-05	0.10±0.02	...	-1.83±0.12	*,2,3
Q0841+129a	1.864	21.00±0.10	...	-0.10±0.12	0.00017±0.04	...	0.0002±0.03	...	...	*,1,3

Table B.1: continued

QSO	$z_{\rm abs}$	log N(H I)	log N(H 2)	[Zn/Fe]	DTM	DTG	DTM$_{\rm N}$	$A_{V,\rm depl}$	[M/H]$_{\rm tot}$	Ref
Q0841+129b	2.375	21.05±0.10	...	0.15±0.03	0.11±0.02	4.00e-05±1.00e-05	0.08±0.02	...	-1.61±0.11	*,1,3
Q0841+129c	2.476	20.80±0.10	...	0.13±0.04	0.17±0.11	5.00e-05±4.00e-05	0.16±0.12	...	-1.65±0.14	*,1,3
Q0918+1636	2.583	20.96±0.05	...	0.72±0.01	0.29±0.04	1.31e-03±9.50e-04	0.23±0.05	0.09±0.07	-0.49±0.31	*,2,3
Q0918+1636	2.412	21.26±0.06	...	0.47±0.29	0.23±0.06	3.65e-03±1.16e-03	0.18±0.06	0.46±0.20	0.05±0.09	*,2,3
Q0933+733	1.479	21.62±0.10	...	0.26±0.02	0.15±0.02	8.00e-05±2.00e-05	0.11±0.02	0.02±0.01	-1.44±0.12	*,2,3
Q0935+417	1.373	20.52±0.10	...	0.18±0.10	0.12±0.03	2.60e-04±1.10e-04	0.08±0.02	0.01±0.01	-0.80±0.16	*,2,3
Q0948+433	1.233	21.62±0.06	...	0.34±0.01	0.18±0.02	2.70e-04±6.00e-05	0.14±0.02	0.08±0.02	-0.97±0.09	*,2,3
Q1010+0003	1.265	21.52±0.07	...	0.44±0.08	0.21±0.03	2.60e-04±9.00e-05	0.16±0.03	0.06±0.02	-1.04±0.13	*,2,3
Q1037-270	2.139	19.70±0.05	...	0.07±0.02	0.08±0.02	...	0.05±0.02	...	...	*,1,3
Q1111-152	3.266	21.30±0.05	...	0.25±0.09	0.13±0.03	4.00e-05±2.00e-05	0.10±0.03	0.010±0.001	-1.66±0.14	*,1,3
Q1117-134	3.350	20.95±0.10	...	0.14±0.06	0.09±0.02	4.00e-05±1.00e-05	0.06±0.02	...	-1.46±0.11	*,1,3
Q1137+3907	0.720	21.10±0.10	...	0.73±0.07	0.31±0.04	3.80e-03±1.31e-03	0.25±0.05	0.35±0.15	-0.06±0.14	*,2,3
Q1157+014	1.944	21.80±0.10	...	0.30±0.01	0.17±0.02	9.00e-05±3.00e-05	0.12±0.03	0.04±0.02	-1.42±0.11	*,1,3
Q1209+093	2.584	21.40±0.10	...	0.45±0.03	0.22±0.03	3.20e-04±1.00e-04	0.17±0.03	0.06±0.02	-0.98±0.13	*,1,3
Q1210+17	1.892	20.63±0.08	...	0.14±0.06	0.11±0.02	2.50e-04±8.00e-05	0.07±0.02	0.010±0.001	-0.78±0.12	*,2,3
Q1215+33	1.999	20.95±0.07	...	0.33±0.07	0.19±0.02	2.00e-04±6.00e-05	0.14±0.03	0.011±0.004	-1.13±0.12	*,2,3
Q1223+178	2.466	21.40±0.10	...	-0.03±0.02	0.06±0.01	2.00e-05±1.00e-05	0.040±0.001	...	-1.64±0.14	*,1,3
Q1232+082	2.338	20.90±0.10	...	0.77±0.14	0.29±0.05	1.07e-03±4.70e-04	0.23±0.06	0.06±0.03	-0.57±0.18	*,2,3
Q1328+307	0.692	21.25±0.10	...	0.48±0.14	0.24±0.04	3.30e-04±1.60e-04	0.19±0.04	0.04±0.02	-1.00±0.19	*,2,3
Q1331+170	1.776	21.15±0.07	...	0.66±0.04	0.29±0.03	2.90e-04±9.00e-05	0.23±0.04	0.03±0.01	-1.14±0.12	*,1,3
Q1354+258	1.420	21.54±0.06	...	0.33±0.09	0.18±0.02	1.32e-03±8.40e-04	0.14±0.03	0.31±0.20	-0.29±0.27	*,2,3
Q1409+095a	2.019	20.65±0.10	...	0.10±0.13	0.08±0.04	2.00e-05±1.00e-05	0.06±0.03	...	-1.70±0.15	*,1,3
Q1425+6039	2.827	20.30±0.04	...	0.44±0.04	0.22±0.02	8.00e-04±1.80e-04	0.17±0.03	0.010±0.003	-0.59±0.09	*,2,3
Q1444+014	2.087	20.25±0.07	18.16±0.14	0.86±0.07	0.34±0.05	1.11e-03±5.10e-04	0.28±0.06	0.01±0.01	-0.63±0.19	*,1,3
Q1451+123a	2.255	20.35±0.10	...	0.27±0.12	0.15±0.03	2.10e-04±9.00e-05	0.11±0.03	...	-1.00±0.15	*,1,3
Q1727+5302	1.031	21.41±0.15	...	0.69±0.24	0.27±0.05	1.86e-03±7.70e-04	0.22±0.06	0.36±0.20	-0.31±0.16	*,2,3
Q1727+5302	0.945	21.16±0.10	...	0.71±0.11	0.29±0.04	3.50e-04±2.40e-04	0.23±0.05	0.04±0.03	-1.06±0.29	*,2,3
Q1755+578	1.971	21.40±0.15	...	0.81±0.07	0.31±0.04	5.16e-03±2.24e-03	0.25±0.05	0.97±0.56	0.08±0.18	*,2,3
Q2116-358	1.996	20.10±0.07	...	0.45±0.09	0.22±0.03	1.67e-03±4.50e-04	0.17±0.04	0.01±0.01	-0.27±0.10	*,1,3
Q2138-444a	2.383	20.60±0.05	...	0.33±0.08	0.19±0.02	2.20e-04±6.00e-05	0.14±0.03	0.006±0.002	-1.07±0.11	*,1,3
Q2138-444b	2.852	20.98±0.05	...	0.02±0.03	0.06±0.01	1.00e-05±3.88e-06	0.03±0.01	...	-1.86±0.10	*,1,3
Q2206-199a	1.921	20.67±0.05	...	0.20±0.01	0.14±0.02	6.20e-04±2.20e-04	0.10±0.02	0.02±0.01	-0.51±0.15	*,1,3
Q2228-3954	2.095	21.20±0.10	...	0.08±0.06	0.06±0.02	5.00e-05±2.00e-05	0.04±0.01	...	-1.26±0.14	*,2,3
Q2230+025	1.864	20.83±0.05	...	0.35±0.07	0.18±0.02	7.60e-04±2.20e-04	0.13±0.03	0.03±0.01	-0.52±0.11	*,2,3
Q2231-00	2.066	20.53±0.08	...	0.21±0.06	0.15±0.02	3.50e-04±1.10e-04	0.10±0.02	0.008±0.003	-0.76±0.12	*,2,3
Q2243-605	2.331	20.65±0.05	...	0.26±0.02	0.16±0.02	3.50e-04±1.10e-04	0.11±0.02	0.010±0.004	-0.79±0.12	*,1,3
Q2318-1107	1.989	20.68±0.05	15.49±0.03	0.34±0.03	0.20±0.02	5.80e-04±1.40e-04	0.15±0.02	0.02±0.01	-0.68±0.09	*,2,3
Q2332-094a	2.287	20.07±0.07	...	0.92±0.04	0.35±0.04	3.09e-03±1.07e-03	0.29±0.06	0.03±0.01	-0.20±0.14	*,1,3
Q2343+125	2.431	20.40±0.07	13.69±0.09	0.39±0.03	0.21±0.02	3.90e-04±1.00e-04	0.16±0.03	0.007±0.002	-0.86±0.10	*,1,3
Q2359-022a	2.095	20.65±0.10	...	0.75±0.08	0.29±0.04	1.19e-03±5.20e-04	0.24±0.05	0.04±0.02	-0.53±0.18	*,1,3
SDSS0225+0054	2.714	21.00±0.15	...	0.33±0.14	0.18±0.03	6.30e-04±3.20e-04	0.14±0.04	0.04±0.03	-0.61±0.21	*,2,3
SDSS1116+4118A	2.662	20.48±0.10	...	0.79±0.22	0.31±0.05	1.47e-03±8.80e-04	0.25±0.06	0.03±0.02	-0.46±0.25	*,2,3
SDSS1249-0233	1.781	21.45±0.15	...	0.42±0.05	0.21±0.02	4.70e-04±1.90e-04	0.15±0.03	0.09±0.05	-0.78±0.17	*,2,3
SDSS1610+4724	2.508	21.15±0.15	...	0.69±0.07	0.28±0.04	4.04e-03±1.76e-03	0.23±0.05	0.42±0.24	0.01±0.18	*,2,3
SDSS2059-0529	2.210	20.80±0.20	...	0.68±0.16	0.30±0.04	2.26e-03±1.39e-03	0.24±0.05	0.10±0.08	-0.26±0.26	*,2,3
SDSS2100-0641	3.092	21.05±0.15	...	0.62±0.07	0.27±0.03	2.23e-03±9.60e-04	0.21±0.04	0.18±0.10	-0.23±0.18	*,2,3
UM673A	1.626	20.70±0.10	...	-0.42±0.15	0.03±0.06	1.00e-05±2.00e-05	0.02±0.05	...	-1.59±0.20	*,2,3
eHAQ0111+0641	2.027	21.50±0.30	...	0.44±0.14	0.22±0.04	1.05e-03±8.40e-04	0.17±0.04	0.23±0.25	-0.47±0.34	*,2,3

References: Measurements of the DTM, DTG, DTM$_{\rm N}$ and $A_{V,\rm depl}$ are from (⋆) this work, column densities from (1) De Cia et al. (2016); (2) Berg et al. (2015) and total dust-corrected metallicities from De Cia et al. (2018).

Table B.2: Milky Way dust properties

Star	log N(H I)	log N(H 2)	[Zn/Fe]	DTM	DTG	DTM$_{\rm N}$	$A_{V,\rm depl}$	[M/H]$_{\rm tot}$	Ref
1-SCO	...	...	1.53±0.21	0.46±0.06	...	0.40±0.08	...	...	*,2
23O-ORI	...	...	1.75±0.08	0.56±0.08	...	0.54±0.08	...	...	*,2
62-TAU	20.95±0.10	20.79±0.10	1.56±0.09	0.47±0.06	2.55e-03±8.30e-04	0.41±0.08	0.44±0.23	-0.41±0.13	*,1
BET-1-SCO	...	...	1.56±0.23	0.52±0.14	...	0.48±0.15	...	...	*,2
CHI-OPH	21.13±0.10	20.63±0.10	1.29±0.04	0.43±0.05	2.80e-03±7.90e-04	0.37±0.07	0.48±0.24	-0.33±0.11	*,1

Table B.2: continued

Star	log N(H I)	log N(H 2)	[Zn/Fe]	DTM	DTG	DTM$_{\rm N}$	$A_{V,\rm depl}$	[M/H]$_{\rm tot}$	Ref
DEL-ORI-A	...	...	1.41±0.08	0.48±0.08	...	0.42±0.09	...	...	*,2
EPS-ORI	...	...	1.61±0.08	0.52±0.07	...	0.47±0.09	...	...	*,2
EPS-PER	20.45±0.10	19.52±0.10	1.38±0.14	0.45±0.06	4.12e-03±1.33e-03	0.39±0.07	0.11±0.06	-0.18±0.13	*,1
HD-110432	20.85±0.10	20.64±0.10	1.51±0.08	0.46±0.06	4.67e-03±1.72e-03	0.40±0.08	0.59±0.33	-0.14±0.15	*,1
HD-116852	...	...	0.84±0.04	0.34±0.04	...	0.27±0.05	...	...	*,2
HD-149404	21.40±0.10	20.79±0.10	1.41±0.09	0.45±0.06	5.68e-03±1.37e-03	0.39±0.07	1.66±0.80	-0.04±0.09	*,1
HD-154368	21.00±0.10	21.16±0.10	1.29±0.04	0.43±0.05	2.28e-03±6.90e-04	0.37±0.07	0.69±0.36	-0.42±0.12	*,1
HD-164402	21.11±0.10	19.49±0.10	1.15±0.04	0.41±0.05	4.00e-03±1.13e-03	0.34±0.07	0.42±0.21	-0.15±0.11	*,1
HD-18100	...	...	0.80±0.06	0.33±0.04	...	0.27±0.05	...	...	*,2
HD-188439	20.78±0.10	19.95±0.10	1.20±0.03	0.41±0.05	6.03e-03±1.22e-03	0.35±0.07	0.36±0.17	0.02±0.07	*,1
HD-199579	21.04±0.10	20.53±0.10	1.65±0.06	0.48±0.06	9.71e-03±3.37e-03	0.42±0.08	1.38±0.75	0.16±0.14	*,1
HD-206267	21.30±0.10	20.86±0.10	1.42±0.12	0.45±0.06	3.84e-03±1.16e-03	0.39±0.07	1.05±0.54	-0.21±0.12	*,1
HD-215733	...	...	0.92±0.13	0.35±0.05	...	0.29±0.06	...	...	*,2
HD-62542	20.70±0.10	20.81±0.10	1.50±0.05	0.46±0.06	2.34e-03±6.60e-04	0.40±0.08	0.33±0.28	-0.44±0.11	*,1
HD-73882	21.11±0.10	21.11±0.10	1.26±0.10	0.42±0.06	2.19e-03±6.30e-04	0.36±0.07	0.67±0.34	-0.43±0.11	*,1
HR-4908	21.08±0.10	20.14±0.10	1.40±0.08	0.45±0.06	6.67e-03±2.02e-03	0.39±0.07	0.78±0.40	0.03±0.12	*,1
IOT-ORI	20.20±0.10	14.69±0.10	1.43±0.10	0.45±0.06	1.200e-02±3.88e-03	0.39±0.07	0.15±0.08	0.28±0.13	*,1
KAP-AQL	20.90±0.10	20.31±0.10	1.28±0.05	0.43±0.05	3.61e-03±1.24e-03	0.37±0.07	0.34±0.18	-0.22±0.14	*,1
KSI-PER	...	...	1.52±0.04	0.41±0.08	...	0.32±0.10	...	...	*,2
LAM-SCO	...	...	1.22±0.07	0.39±0.09	...	0.33±0.10	...	...	*,2
MU-COL	...	...	1.13±0.08	0.42±0.05	...	0.36±0.06	...	...	*,2
OMI-PER	20.82±0.10	20.60±0.10	1.40±0.09	0.45±0.06	2.54e-03±1.10e-03	0.39±0.07	0.29±0.17	-0.39±0.18	*,1
PI-SCO	...	...	1.53±0.10	0.47±0.06	...	0.41±0.08	...	...	*,2
RHO-OPH-A	21.63±0.10	20.57±0.10	1.19±0.07	0.41±0.05	9.50e-04±2.90e-04	0.35±0.07	0.37±0.19	-0.78±0.12	*,1
TAU-CMA	...	...	1.33±0.10	0.50±0.09	...	0.46±0.10	...	...	*,2
TET-MUS	21.15±0.10	19.83±0.10	1.32±0.04	0.43±0.06	8.48e-03±2.24e-03	0.37±0.07	1.03±0.51	0.15±0.10	*,1
TET01-ORI-C	21.54±0.10	17.25±0.10	1.04±0.05	0.38±0.05	1.69e-03±8.00e-04	0.32±0.06	0.44±0.28	-0.50±0.20	*,1
V600-HER	...	...	0.84±0.08	0.34±0.04	...	0.28±0.05	...	...	*,2
X-PER	20.73±0.1	20.92±0.10	1.33±0.05	0.44±0.05	1.68e-03±4.10e-04	0.37±0.07	0.29±0.14	-0.56±0.09	*,1
ZET-OPH	...	...	1.65±0.06	0.47±0.07	...	0.41±0.09	...	...	*,2
ZET-ORI-A	20.39±0.10	15.86±0.10	1.41±0.10	0.45±0.06	8.99e-03±2.17e-03	0.39±0.07	0.17±0.08	0.16±0.09	*,1
ZET-PUP	...	...	1.21±0.21	0.39±0.06	...	0.34±0.07	...	...	*,2

References: Measurements of the DTM, DTG, DTM$_{\rm N}$ and $A_{V,\rm depl}$ are from (⋆) this work, column densities from (1) De Cia et al. (2021); (2) Jenkins (2009) and total dust-corrected metallicities from De Cia et al. (2021).

Table B.3: LMC dust properties

Star	log N(H I)	log N(H 2)	[Zn/Fe]	DTM	DTG	DTM$_{\rm N}$	$A_{V,\rm depl}$	[M/H]$_{\rm tot}$	Ref
BI173	21.25±0.05	15.64±0.10	0.83±0.05	0.34±0.04	1.54e-03±3.00e-04	0.28±0.05	0.20±0.05	-0.49±0.07	*,1,2
BI184	21.15±0.04	19.65±0.10	0.73±0.08	0.32±0.04	1.86e-03±4.80e-04	0.26±0.05	0.19±0.06	-0.38±0.10	*,1,2
BI237	21.65±0.03	20.05±0.10	0.98±0.07	0.37±0.05	1.65e-03±2.50e-04	0.31±0.06	0.56±0.12	-0.50±0.04	*,1,2
BI253	21.68±0.03	19.76±0.10	0.83±0.04	0.34±0.04	1.39e-03±1.90e-04	0.27±0.05	0.49±0.10	-0.53±0.03	*,1,2
PGMW3120	21.48±0.03	18.30±0.10	0.97±0.08	0.37±0.05	1.64e-03±4.00e-04	0.31±0.06	0.37±0.11	-0.50±0.09	*,1,2
PGMW3223	21.40±0.06	18.69±0.10	1.03±0.06	0.39±0.05	2.71e-03±7.00e-04	0.32±0.06	0.51±0.17	-0.30±0.10	*,1,2
SK 6522	20.66±0.03	14.93±0.10	0.83±0.06	0.33±0.04	3.36e-03±6.70e-04	0.27±0.05	0.11±0.03	-0.14±0.07	*,1,2
SK 66172	21.27±0.03	18.21±0.10	1.11±0.06	0.40±0.05	1.91e-03±4.30e-04	0.33±0.06	0.27±0.08	-0.46±0.08	*,1,2
SK-6619	21.87±0.07	20.20±0.10	1.25±0.13	0.42±0.06	2.28e-03±8.90e-04	0.36±0.07	1.31±0.59	-0.41±0.16	*,1,2
SK 6635	20.85±0.04	19.30±0.10	0.84±0.14	0.34±0.05	4.19e-03±1.47e-03	0.27±0.06	0.22±0.09	-0.05±0.14	*,1,2
SK 67101	20.20±0.04	14.14±0.10	0.68±0.13	0.31±0.04	5.45e-03±2.00e-03	0.25±0.05	0.06±0.03	0.10±0.15	*,1,2
SK 67105	21.26±0.04	19.13±0.10	0.86±0.07	0.21±0.16	5.00e-04±3.90e-04	0.14±0.17	0.05±0.07	-0.77±0.09	*,1,2
SK-67191	20.78±0.03	14.28±0.10	0.52±0.20	0.24±0.05	1.09e-03±6.20e-04	0.19±0.06	0.05±0.03	-0.49±0.23	*,1,2
SK 672	21.46±0.12	20.95±0.10	1.15±0.11	0.41±0.05	8.40e-04±1.70e-04	0.35±0.07	0.19±0.07	-0.83±0.07	*,1,2
SK 67211	20.81±0.04	13.98±0.10	0.73±0.06	0.31±0.04	3.77e-03±5.80e-04	0.25±0.05	0.18±0.04	-0.06±0.04	*,1,2
SK 675	21.04±0.04	19.46±0.10	1.00±0.05	0.37±0.05	1.76e-03±2.70e-04	0.31±0.06	0.15±0.03	-0.47±0.04	*,1,2
SK 68129	21.62±0.14	20.20±0.10	1.33±0.14	0.44±0.05	4.51e-03±2.15e-03	0.37±0.07	1.47±0.87	-0.13±0.20	*,1,2
SK 68135	21.48±0.02	19.87±0.10	1.04±0.07	0.39±0.05	1.66e-03±2.30e-04	0.32±0.06	0.38±0.08	-0.51±0.03	*,1,2
SK 68140	21.51±0.11	20.11±0.10	1.16±0.10	0.41±0.05	4.11e-03±1.60e-03	0.34±0.07	1.03±0.50	-0.14±0.16	*,1,2
SK 68155	21.47±0.09	19.99±0.10	1.06±0.05	0.39±0.05	4.13e-03±1.16e-03	0.33±0.06	0.93±0.35	-0.12±0.11	*,1,2
SK 6826	21.65±0.06	20.38±0.10	1.05±0.15	0.38±0.05	9.00e-04±3.70e-04	0.32±0.07	0.31±0.14	-0.77±0.17	*,1,2
SK 6852	21.31±0.06	19.47±0.10	0.43±0.12	0.21±0.04	1.59e-03±2.80e-04	0.16±0.04	0.23±0.06	-0.27±0.03	*,1,2

SK 6873	21.68±0.02	20.09±0.10	1.24±0.12	0.38±0.12	3.48e-03±1.08e-03	0.31±0.13	1.25±0.53	-0.18±0.03	*,1,2
SK 69104	19.57±0.68	14.03±0.10	1.06±0.27	0.39±0.06	1.36e-02±2.30e-02	0.32±0.07	0.04±0.09	0.40±0.73	*,1,2
SK 69175	20.64±0.03	14.28±0.10	0.38±0.12	0.20±0.03	8.00e-04±2.70e-04	0.15±0.04	0.02±0.01	-0.55±0.13	*,1,2
SK 69246	21.48±0.02	19.71±0.10	0.80±0.04	0.33±0.04	1.81e-03±2.30e-04	0.27±0.05	0.40±0.08	-0.41±0.02	*,1,2
SK 69279	21.63±0.05	20.31±0.10	0.76±0.06	0.32±0.04	7.20e-04±1.60e-04	0.26±0.05	0.22±0.07	-0.79±0.08	*,1,2
SK 70115	21.18±0.08	19.94±0.10	0.67±0.05	0.30±0.03	2.02e-03±2.50e-04	0.23±0.04	0.22±0.06	-0.31±0.02	*,1,2
SK 7079	21.34±0.04	20.26±0.10	1.51±0.09	0.39±0.09	4.48e-03±1.67e-03	0.32±0.10	0.74±0.33	-0.08±0.13	*,1,2
SK 7145	21.11±0.03	18.63±0.10	0.81±0.06	0.34±0.04	2.81e-03±5.60e-04	0.27±0.05	0.27±0.07	-0.22±0.07	*,1,2
SK 7150	21.24±0.05	20.13±0.10	0.55±0.05	0.28±0.03	1.42e-03±2.80e-04	0.22±0.04	0.17±0.05	-0.44±0.07	*,1,2

References: Measurements of the DTM, DTG, $\mathrm{DTM_N}$, and $A_{V,\mathrm{depl}}$ are from (★) this work, column densities from (1) Roman-Duval et al. (2021); and total dust-corrected metallicities from (2) De Cia et al. in prep.

Table B.4: SMC dust properties

Star	log N(H I)	log N(H 2)	[Zn/Fe]	DTM	DTG	$\mathrm{DTM_N}$	$A_{V,\mathrm{depl}}$	$[\mathrm{M/H}]_{\mathrm{tot}}$	Ref
AzV18	22.04±0.02	20.36±0.08	0.91±0.09	0.35±0.04	1.07e-03±1.60e-04	0.29±0.06	0.92±0.20	-0.66±0.03	*,1,2
AzV26	21.70±0.06	20.63±0.06	0.60±0.05	0.28±0.03	4.10e-04±5.00e-05	0.22±0.04	0.17±0.04	-0.98±0.02	*,1,2
AzV47	21.32±0.04	18.54±0.70	0.57±0.07	0.27±0.03	6.90e-04±1.00e-04	0.21±0.04	0.10±0.02	-0.73±0.03	*,1,2
AzV80	21.81±0.02	20.08±0.30	0.69±0.06	0.30±0.04	6.40e-04±9.00e-05	0.24±0.05	0.31±0.07	-0.81±0.02	*,1,2
AzV95	21.49±0.04	19.40±0.09	0.57±0.07	0.27±0.03	5.30e-04±8.00e-05	0.21±0.04	0.12±0.03	-0.84±0.03	*,1,2
AzV104	21.45±0.06	19.23±0.30	0.51±0.16	0.23±0.04	3.90e-04±1.80e-04	0.18±0.05	0.08±0.04	-0.92±0.19	*,1,2
AzV207	21.43±0.06	19.40±0.10	0.83±0.06	0.34±0.04	1.66e-03±2.50e-04	0.27±0.05	0.34±0.08	-0.45±0.04	*,1,2
AzV216	21.64±0.03	18.78±1.30	0.72±0.08	0.30±0.04	7.20e-04±1.70e-04	0.24±0.05	0.23±0.07	-0.77±0.09	*,1,2
AzV229	21.06±0.04	15.66±0.30	0.62±0.08	0.25±0.03	8.30e-04±1.30e-04	0.20±0.04	0.07±0.02	-0.62±0.03	*,1,2
AzV242	21.32±0.04	17.21±1.30	1.16±0.18	0.41±0.06	1.37e-03±2.30e-04	0.35±0.07	0.22±0.05	-0.62±0.04	*,1,2
AzV321	20.70±0.08	14.44±1.30	0.90±0.11	0.35±0.05	2.07e-03±3.60e-04	0.29±0.06	0.08±0.02	-0.37±0.05	*,1,2
AzV332	20.54±0.16	14.50±0.12	0.56±0.06	0.26±0.03	1.20e-03±5.00e-04	0.20±0.04	0.03±0.02	-0.47±0.17	*,1,2
AzV388	21.18±0.04	19.40±0.10	0.99±0.07	0.35±0.05	1.36e-03±2.60e-04	0.30±0.06	0.16±0.04	-0.56±0.06	*,1,2
AzV456	21.00±0.06	20.93±0.10	1.36±0.09	0.44±0.06	5.00e-04±1.00e-04	0.38±0.07	0.11±0.03	-1.09±0.07	*,1,2
AzV476	21.85±0.07	20.95±0.30	0.81±0.17	0.33±0.04	5.20e-04±2.50e-04	0.27±0.05	0.34±0.18	-0.95±0.20	*,1,2
AzV327	20.93±0.10	14.79±0.10	0.93±0.19	0.36±0.05	3.00e-04±2.00e-04	0.30±0.06	0.09±0.08	-1.23±0.29	*,1,2
AzV238	21.41±0.10	15.95±0.10	0.99±0.04	0.38±0.05	1.04e-03±5.40e-04	0.31±0.06	0.20±0.15	-0.70±0.22	*,1,2
SK116	21.57±0.10	18.53±0.10	0.64±0.04	0.29±0.03	5.50e-04±2.90e-04	0.23±0.04	0.15±0.11	-0.86±0.22	*,1,2

References: Measurements of the DTM, DTG, $\mathrm{DTM_N}$, and $A_{\mathrm{V,depl}}$ are from (★) this work, column densities from (1) Jenkins & Wallerstein (2017); and total dust-corrected metallicities from (2) De Cia et al. in prep.

Table B.5: GRB-DLAs dust properties

GRB	z_{abs}	log N(H I)	log N(H 2)	[Zn/Fe]	DTM	DTG	DTM_N	$A_{V,depl}$	$[M/H]_{tot}$	Ref
00926	2.0380	21.30±0.20	...	1.06±0.18	0.39±0.05	8.55e-03±5.63e-03	0.32±0.07	1.30±1.00	0.20±0.28	*,1
030226	1.9870	20.50±0.30	...	-0.18±0.12	...	...	...	...	-1.07±0.31	*,1
050730	3.9690	22.10±0.10	...	0.08±0.05	0.06±0.02	4.00e-06±2.00e-06	0.04±0.01	...	-2.31±0.18	*,1
050820A	2.6150	21.05±0.10	...	0.83±0.05	0.34±0.04	1.53e-03±3.92e-04	0.27±0.05	0.13±0.06	-0.49±0.10	*,1
050922C	2.1990	21.55±0.10	...	0.18±0.46	0.12±0.11	1.94e-05±2.20e-05	0.08±0.10	0.005±0.006	-1.92±0.26	*,1
071031	2.6920	22.15±0.05	...	0.04±0.03	0.03±0.01	7.70e-06±3.70e-06	0.02±0.01	0.007±0.004	-1.75±0.09	*,1
080413A	2.4330	21.85±0.15	...	0.13±0.07	0.09±0.02	3.02e-05±1.49e-05	0.06±0.02	0.01±0.01	-1.60±0.18	*,1
081008	1.9685	21.11±0.10	...	0.55±0.04	0.26±0.03	1.12e-03±4.61e-04	0.20±0.04	0.10±0.06	-0.51±0.17	*,1
090809A	2.7373	21.48±0.07	...	0.75±0.21	0.32±0.05	1.54e-03±5.85e-04	0.26±0.06	0.34±0.19	-0.46±0.15	*,1
090926A	2.1069	21.58±0.01	...	0.88±0.11	0.34±0.05	8.99e-05±1.59e-05	0.28±0.06	0.03±0.01	-1.72±0.05	*,1
100219A	4.6676	21.28±0.02	...	0.12±0.30	0.07±0.08	7.12e-05±8.05e-05	0.05±0.07	0.01±0.01	-1.16±0.11	*,1
111008A	4.9910	22.39±0.01	...	0.22±0.10	0.13±0.02	2.87e-05±8.60e-06	0.09±0.02	0.05±0.02	-1.79±0.10	*,1
111107A	2.8930	21.10±0.04	...	0.70±0.55	0.30±0.09	2.22e-03±2.40e-03	0.24±0.10	0.20±0.24	-0.28±0.45	*,1
120119A	1.7285	22.44±0.12	...	0.93±0.24	0.36±0.06	8.16e-04±7.99e-04	0.30±0.07	1.69±1.78	-0.79±0.42	*,1
120327A	2.8143	22.07±0.01	17.39±0.13	0.27±0.07	0.15±0.03	9.78e-05±1.99e-05	0.11±0.03	0.08±0.03	-1.34±0.02	*,1
120716A	2.4874	21.73±0.03	...	0.69±0.23	0.31±0.05	1.15e-03±2.84e-04	0.24±0.06	0.45±0.21	-0.57±0.08	*,1
120815A	2.3582	22.09±0.01	20.42±0.08	1.01±0.05	0.38±0.05	3.10e-04±4.30e-05	0.31±0.06	0.30±0.12	-1.23±0.03	*,1
120909A	3.9290	21.82±0.02	...	1.15±0.09	0.41±0.05	2.90e-03±7.62e-04	0.34±0.07	1.48±0.68	-0.29±0.10	*,1
121024A	2.3005	21.78±0.02	19.90±0.17	0.77±0.08	0.31±0.04	8.95e-04±1.87e-04	0.25±0.05	0.41±0.18	-0.68±0.07	*,1
130408A	3.7579	21.90±0.01	...	0.29±0.07	0.17±0.02	7.99e-05±1.43e-05	0.12±0.03	0.04±0.02	-1.46±0.05	*,1
130606A	5.9127	19.88±0.01	...	0.49±0.10	0.24±0.03	8.87e-05±1.99e-05	0.19±0.04	...	-1.58±0.08	*,1
140311A	4.9550	22.30±0.02	...	0.35±0.21	0.20±0.05	2.76e-05±9.80e-06	0.14±0.05	0.04±0.02	-2.00±0.11	*,1
141028A	2.3333	20.39±0.03	...	-0.04±0.26	0.001±0.090	4.00e-07±2.91e-05	0.001±0.062	...	-1.62±0.28	*,1
141109A	2.9940	22.18±0.02	18.02±0.12	0.49±0.07	0.24±0.03	1.45e-04±2.46e-05	0.19±0.04	0.15±0.06	-1.37±0.05	*,1
150403A	2.0571	21.73±0.02	19.90±0.14	0.63±0.08	0.29±0.04	4.84e-04±8.28e-05	0.23±0.04	0.19±0.08	-0.92±0.05	*,1
151021A	2.3297	22.14±0.03	18.99±1.28	0.86±0.08	0.35±0.05	5.20e-04±1.07e-04	0.28±0.06	0.53±1.02	-0.97±0.07	*,1
151027B	4.0650	20.54±0.07	...	0.49±0.64	0.24±0.12	8.67e-04±6.78e-04	0.19±0.12	0.02±0.02	-0.59±0.27	*,1
160203A	3.5187	21.74±0.02	...	0.37±0.18	0.19±0.04	3.25e-04±7.45e-05	0.15±0.04	0.12±0.06	-0.92±0.04	*,1
161023A	2.7100	20.95±0.01	...	0.44±0.04	0.22±0.02	2.76e-04±3.77e-05	0.17±0.03	0.02±0.01	-1.05±0.04	*,1
170202A	3.6456	21.53±0.04	...	0.75±0.23	0.32±0.05	4.24e-04±1.44e-04	0.26±0.06	0.11±0.05	-1.02±0.13	*,1
181020A	2.9379	22.24±0.03	...	0.75±0.14	0.32±0.04	2.80e-04±6.48e-05	0.26±0.06	0.36±0.16	-1.20±0.08	*,1
190114A	3.3764	22.19±0.05	...	1.05±0.08	0.39±0.05	3.64e-04±6.69e-05	0.32±0.06	0.43±0.18	-1.17±0.06	*,1
190106A	1.8599	21.00±0.04	...	1.12±0.10	0.40±0.05	2.19e-03±5.77e-04	0.33±0.06	0.17±0.08	-0.40±0.10	*,1
190919B	3.2241	21.75±0.06	...	0.33±0.33	0.18±0.07	1.43e-04±7.45e-05	0.14±0.07	0.05±0.04	-1.25±0.15	*,1
191011A	1.7204	21.65±0.08	...	0.33±0.09	0.18±0.02	5.97e-04±1.22e-04	0.14±0.03	0.18±0.08	-0.63±0.07	*,1
210905A	6.3118	21.10±0.10	...	0.33±0.09	0.18±0.02	4.85e-05±1.57e-05	0.14±0.03	...	-1.72±0.13	*,1

References: (⋆) This work; (1) Heintz et al. (2023)